Icarus 202 (2009) 525–542

Contents lists available at ScienceDirect

Icarus

www.elsevier.com/locate/icarus

The deep wind structure of the giant planets: Results from an anelastic general circulation model

Yohai Kaspi [a,*], Glenn R. Flierl [a], Adam P. Showman [b]

[a] Department of Earth, Atmospheric and Planetary Sciences, Massachusetts Institute of Technology, 77 Massachusetts Ave., Cambridge, MA 02139-4307, USA
[b] Lunar and Planetary Laboratory, University of Arizona, Tucson, AZ 85721-0092, USA

ARTICLE INFO

Article history:
Received 3 November 2008
Revised 24 February 2009
Accepted 8 March 2009
Available online 25 March 2009

Keywords:
Jovian planets
Jupiter, atmosphere
Jupiter, interior

ABSTRACT

The giant gas planets have hot convective interiors, and therefore a common assumption is that these deep atmospheres are close to a barotropic state. Here we show using a new anelastic general circulation model that baroclinic vorticity contributions are not negligible, and drive the system away from an isentropic and therefore barotropic state. The motion is still aligned with the direction of the axis of rotation as in a barotropic rotating fluid, but the wind structure has a vertical shear with stronger winds in the atmosphere than in the interior. This shear is associated with baroclinic compressibility effects. Most previous convection models of giant planets have used the Boussinesq approximation, which assumes the density is constant in depth; however, Jupiter's actual density varies by four orders of magnitude through its deep molecular envelope. We therefore developed a new general circulation model (based on the MITgcm) that is anelastic and thereby incorporates this density variation. The model's geometry is a full 3D sphere down to a small inner core. It is nonhydrostatic, uses an equation of state suitable for hydrogen–helium mixtures (SCVH), and is driven by an internal heating profile. We demonstrate the effect of compressibility by comparing anelastic and Boussinesq cases. The simulations develop a mean state that is geostrophic and hydrostatic including the often neglected, but significant, vertical Coriolis contribution. This leads to modification of the standard thermal wind relation for a deep compressible atmosphere. The interior flow organizes in large cyclonically rotating columnar eddies parallel to the rotation axis, which drive upgradient angular momentum eddy fluxes, generating the observed equatorial superrotation. Heat fluxes align with the axis of rotation, and provide a mechanism for the transport of heat poleward, which can cause the observed flat meridional emission. We address the issue of over-forcing which is common in such convection models and analyze the dependence of our results on this; showing that the vertical wind structure is not very sensitive to the Rayleigh number. We also study the effect of rotation, showing how the transition from a rapidly to a slowly rotating system affects the dynamics.

1. Introduction

One of the most fundamental open questions regarding the atmospheres of the gas giant planets is how deep are the strong winds which are observed in their atmospheres. The winds in the atmospheres of both Jupiter and Saturn are predominantly zonal, reaching 140 $m\,s^{-1}$ on Jupiter (Ingersoll, 1990; Porco et al., 2003) and nearly 400 $m\,s^{-1}$ on Saturn (Porco et al., 2005). The winds near the equator on both planets are superrotating (eastward), reaching approximately latitude 17° on Jupiter, and latitude 30° on Saturn, roughly symmetric around the equator. Traditionally there have been two essentially decoupled approaches treating the formation of the zonal winds on the giant planets (see Vasavada and Showman, 2005, for a review). The first, based on shallow-water turbulence theory (Rhines, 1975) suggests that the jets emerge from geostrophic turbulence on a rotating sphere (Williams, 1978, 1979; Cho and Polvani, 1996; Smith, 2003; Kaspi and Flierl, 2007; Showman, 2007; Scott and Polvani, 2007), while the other approach (Busse, 1970, 1976) claimed the zonal surface velocities are surface manifestation of concentric rotating cylinders (Taylor columns) penetrating the depth of the planet, and that their interactions are creating the zonal jets. Thus one approach suggested that the jets are shallow (thus constraint to a thin weather-layer) and result from shallow geostrophic turbulence, while the other approach suggested that they are deep (thus penetrating deep into the interior of the planet) and result from deep rotating cylinders. However the source of the forcing (whether deep or shallow) may be decoupled from whether the zonal winds

* Corresponding author. Current address: Division of Geological and Planetary Sciences, California Institute of Technology, MC-100-23, Pasadena, CA 91125, United States.

E-mail addresses: yohai@caltech.edu (Y. Kaspi), glenn@lake.mit.edu (G.R. Flierl), showman@lpl.arizona.edu (A.P. Showman).

0019-1035/$ – see front matter
doi:10.1016/j.icarus.2009.03.026

are deep or shallow (Haynes et al., 1991; Showman et al., 2006; Lian and Showman, 2008). Showman et al. (2006) and Lian and Showman (2008) suggest that deep jets on giant planets might result from shallow forcing, and here we suggest that baroclinic jets which are stronger near the surface can result from deep forcing.

Observational evidence of the deep flows on Jupiter is very limited (Ingersoll et al., 2004). The only direct observation is from the *Galileo* probe, which showed an increase in zonal velocity from 80 $\mathrm{m\,s^{-1}}$ to 160 $\mathrm{m\,s^{-1}}$ down to the 4 bar level and then a constant wind speed down to the 24 bar level (Atkinson et al., 1996). Nevertheless the probe entered a "hot spot" which may not be a good representation of the general flow (Orton et al., 1998; Showman and Dowling, 2000). Indirect observations of the subcloud level winds using cloud tracked wind velocities have been inferred by Dowling and Ingersoll (1988) and Dowling and Ingersoll (1989) who suggest based on arguments of conservation of potential vorticity that there must be nonzero zonal winds underlying the great red spot. Conrath et al. (1981) and Gierasch et al. (1986) use thermal wind arguments to show that deep wind are expected beneath the cloud level. However we note that both direct and indirect observations are constrained to a very small fraction of the radius of the planet (the 22 bar level where the Galileo probe was lost is about 0.2% of the radius of the planet), and therefore in the context of this study are considered shallow.

The heat emission on both Jupiter and Saturn has a nearly uniform meridional structure (Ingersoll, 1976; Hanel et al., 1981, 1983) suggesting deep transfer of heat indicating possibly deep flows (Ingersoll and Porco, 1978). Kirk and Stevenson (1987) and Liu et al. (2007) put constraints on the possible extent of deep flows based on the ohmic dissipation created by the zonal flows in an electrically conducting fluid by the magnetic field. Liu et al. (2007) suggest that if the zonal flows in the interior would be as strong as they are on the surface, and the magnetic field can also be deduced by the surface values, then the zonal winds could not penetrate more than 0.95 and 0.87 of the radius on Jupiter and Saturn respectively. In this study we do not include the effect of the magnetic field, however we show that even without the magnetic field acting to dissipate the flow in the interior, interior velocities are weaker than exterior ones as a result of the big radial increase in density. Still, vertical shear due to compressibility does not totally suppress the zonal velocity in the interior.

Several models have shown formation of zonal winds driven by convection in rotating deep spherical shells. Most previous models however have been restricted to using the Boussinesq approximation. Sun et al. (1993), Zhang and Schubert (1996), Aurnou and Olson (2001) and Christensen (2002) show numerical experiments of uniform density fluids with zonal patterns appearing on the surface. In some cases these bands were not steady and weaker than the meridional flows. Heimpel et al. (2005) and Heimpel and Aurnou (2007) show superrotating equatorial zonal flow, with higher latitude meridionally confined jets in a Boussinesq model, where the zonal velocities persist throughout the depth of the planet and the meridional extent of the equatorial superrotating jet seems to be set by the location of the bottom boundary.

Clearly, for addressing the vertical structure of the zonal winds we must allow density variations over the depth of the planet. In this work we use the anelastic approximation allowing the mean density to vary by more than four orders of magnitude from top to bottom. In addition we use an equation of state appropriate for high pressure hydrogen and helium mixtures (SCVH) (Saumon et al., 1995). We try to decouple our results from the choice of the location of the bottom boundary and therefore push it deep below what is believed to be the boundary of the molecular fluid. To the best of our knowledge no other published model attempted to solve for the full 3D nonhydrostatic dynamics including a realistic density variation and a suitable equation of state. Other attempts using the anelastic approximation (Evonuk and Glatzmaier, 2006; Evonuk, 2008) were limited to 2D cases where they show how expansion of a rising convecting fluid due to the density stratification can drive differential rotation on the equatorial plane. Other 3D general circulation models for Jupiter (cf. Yamazaki et al., 2004; Dowling et al., 2006) were hydrostatic and confined to atmospheric shallow type systems.

Based on emission measurements and on theoretical models it is believed that the deep atmosphere is convective (Hubbard, 1984; Guillot, 2005). A common assumption is that if the interior is convective it is close to a purely barotropic state. This is based on the assumption that convective mixing homogenizes the entropy, and causes uniform mixing limiting the density variations on constant pressure surfaces. We note two points: First convection tends to form plumes meaning that even if the atmosphere is driven by strong convection, since the regions of strong upwelling plumes tend to be very localized (Lindzen, 1977) much of the atmosphere may be slightly stably stratified with small regions of convectively unstable plumes, and the atmosphere can still have horizontal density gradients. Earth's tropical atmosphere is an example of such a case. Secondly, the density anomalies are not just a function of entropy (or temperature) anomalies, but must include a second thermodynamical variable. Expressing the density variation in terms of entropy and pressure we find that the pressure gradients contribute significantly to the density gradients, and thus giving a big baroclinic contribution. We find that the baroclinic shear is caused mainly by these compressible effects.

We begin in Section 2 by reviewing the anelastic system. We show that the form of the anelastic system we use is equivalent to other forms such that of Ingersoll and Pollard (1982), and thus is not limited to a specific form of the equation of state. In Section 3 we introduce the new general circulation model, and discuss how it is applied to the giant planets including a realistic reference state, equation of state, and forcing profile. We present the numerical results in Section 4 beginning with demonstrating the effects of compressibility on the dynamics by comparing the zonal velocity structure from the anelastic results to the results limited to Boussinesq dynamics. Then we analyze the basic balances using the numerical results, and show the differences when considering a deep atmosphere rather than one restricted to a thin spherical shell. We focus on the vorticity balance showing both barotropic and baroclinic limits, and show that in the anelastic convective system baroclinic contributions are important, so that compressible baroclinic effects cause zonal wind shear in the direction of the axis of rotation.

In Section 5 we analyze the angular momentum and heat flux budgets, and show the roles of eddy versus mean fluxes in driving the circulation. We find that angular momentum eddy fluxes play an important role in transporting angular momentum to the equator and forming the equatorial superrotating zonal flows. We show the details of the interior circulation including the formation of large scale columnar structures, which have been suggested in qualitative studies (Busse, 1976), but here we show them explicitly in a fully turbulent 3D model. The numerical results show that the convectively driven flow in steady state is in a state in between having Taylor columns, thus constant zonal velocity along the direction of the rotation axis, and constant momentum ($\tilde{\rho}u$) along this direction. Then we further discuss the role of rotation, showing that the character of the flow, and the direction of the equatorial zonal velocity, can be characterized by a single nondimensional number. In Section 6 we use scaling arguments to better relate the results of the numerical model to convection on Jupiter. Particularly we discuss the issue of over-forcing, and show that for the parameter regime studied the baroclinic structure of the velocity is independent of the Rayleigh number.

2. The anelastic system

The anelastic approximation was first introduced by Batchelor (1953) for a adiabatically stratified, horizontally uniform reference state. Then it was more rigorously presented by Ogura and Phillips (1962) in order to filter sound waves in a nonhydrostatic system. They perform a linearization around a specified isentropic state ($\tilde{s}$) which defines a radially dependent reference pressure $\tilde{p}(r)$ and density $\tilde{\rho}(r)$. The mass equation loses the $\partial\rho/\partial t$ term (thereby eliminating the fast sound waves); Ogura and Phillips showed that with suitable changes in other equations and using an ideal gas, the anelastic system conserves energy. Durran (1989) showed a more general solution which he called the pseudo-incompressible approximation, where he relaxes the assumption that entropy anomalies are small compared to the reference adiabatic state. In the pseudo-incompressible system density fluctuations which arise through fluctuations in pressure are neglected, and density fluctuations from temperature are figured into the mass balance. We show that for a convective system the pressure fluctuations are important in the vorticity balance and therefore cannot be neglected. Both the Ogura and Phillips and the pseudo-incompressible formulations treat the fluid as an ideal gas, which is suitable for the atmospheres of the giant planets, but for the interior the fluid diverges significantly from an ideal gas (Guillot, 2005). Ingersoll and Pollard (1982) show that for an isentropic reference state the anelastic system can be applied for a general equation of state. Below we review the anelastic approximation as applied to the model (more details are given in Kaspi, 2008), and show that this form of the anelastic system coincides with that of Ingersoll and Pollard (1982) and therefore can be applied for a general equation of state.

We begin with the momentum equations for a rotating fluid given by

$$\frac{\partial \mathbf{u}}{\partial t} + (2\Omega + \boldsymbol{\omega}) \times \mathbf{u} = -\frac{1}{\rho}\nabla p - \nabla\left(\frac{1}{2}\mathbf{u}^2 + \Phi\right) + \nu\nabla^2\mathbf{u}, \tag{1}$$

where $\mathbf{u}$ is the 3D velocity vector, $\boldsymbol{\omega}$ is the vorticity vector ($\boldsymbol{\omega} = \nabla \times \mathbf{u}$), Ω is the planetary rotation vector, Φ is the gravitational potential ($\nabla\Phi = \mathbf{g}$), ν is the eddy viscosity, and p and ρ are the pressure and density fields respectively (Pedlosky, 1987). We define a basic state which is hydrostatic so that

$$\nabla\tilde{p} = -\tilde{\rho}\nabla\Phi, \tag{2}$$

where the symbol $\tilde{(\cdot)}$ in Eq. (2) denotes the radially dependent reference density and pressure. The temporal and spatial variations from this mean state are denoted with a prime (ρ', p'), and are assumed to be smaller than the mean state, so that the total density and pressure are defined as

$$\rho = \tilde{\rho}(r) + \rho'(\phi, \theta, r, t), \tag{3}$$

$$p = \tilde{p}(r) + p'(\phi, \theta, r, t), \tag{4}$$

where ϕ is the longitude, θ is the latitude and r is the radial coordinate. Unlike the Boussinesq system, the mean density does vary radially. Then to the leading order the momentum equation becomes

$$\frac{\partial \mathbf{u}}{\partial t} + (2\Omega + \boldsymbol{\omega}) \times \mathbf{u} = -\frac{1}{\tilde{\rho}}\nabla p' - \frac{\rho'}{\tilde{\rho}}\nabla\Phi - \frac{1}{2}\nabla\mathbf{u}^2 + \nu\nabla^2\mathbf{u}. \tag{5}$$

We define the basic reference hydrostatic state to be isentropic. This assumption is supported by observational evidence from the *Galileo* probe (Seiff et al., 1997) which find the atmosphere to be close to adiabatic, and calculations of Guillot and Morel (1995) which find the interiors of the giant planets to be close to a purely convective state. We allow fluctuations in entropy, density and pressure from the isentropic reference state, applying therefore a general equation of state (more detail in Kaspi, 2008). Expressing density as function of entropy and pressure $\rho = (s, p)$ then gives

$$\nabla\tilde{\rho} = \left(\frac{\partial\rho}{\partial s}\right)_p \nabla\tilde{s} + \left(\frac{\partial\rho}{\partial p}\right)_s \nabla\tilde{p} = \left(\frac{\partial\rho}{\partial p}\right)_s \nabla\tilde{p} = -\tilde{\rho}\left(\frac{\partial\rho}{\partial p}\right)_s \nabla\Phi, \tag{6}$$

where $\nabla\tilde{s} = 0$ since we assumed an isentropic reference state. Expanding around the reference state gives

$$\frac{\rho'}{\tilde{\rho}} = \frac{1}{\tilde{\rho}}\left(\frac{\partial\rho}{\partial s}\right)_p s' + \frac{1}{\tilde{\rho}}\left(\frac{\partial\rho}{\partial p}\right)_s p' \equiv -\alpha_s s' + \beta p', \tag{7}$$

where the coefficients α_s and β vary radially based on the equation of state (Section 3.1) and $\tilde{\rho}(r)$. Then by using Eqs. (6), (7) the momentum equation (5) can be written as

$$\frac{\partial \mathbf{u}}{\partial t} + (2\Omega + \boldsymbol{\omega}) \times \mathbf{u} = -\nabla P' + \alpha_s s'\nabla\Phi - \frac{1}{2}\nabla\mathbf{u}^2 + \nu\nabla^2\mathbf{u}, \tag{8}$$

where P' is the anelastic potential defined as

$$P' = \frac{p'}{\tilde{\rho}}. \tag{9}$$

This form shows the resemblance of the anelastic system to the Boussinesq system. In the anelastic-isentropic system the natural variable for buoyancy is entropy, rather than density, due to the constant background entropy (rather than density in the Boussinesq system). In addition the anelastic potential (9) is defined instead of the pure pressure anomaly as in the Boussinesq system. A similar system obtained by using directly entropy and temperature instead of pressure and density in Eq. (5) was shown by Ingersoll and Pollard (1982), where the similarity to Eq. (8) can be seen by noting that for the isentropic case, using the appropriate Maxwell relations gives

$$\nabla\tilde{T} = \left(\frac{\partial T}{\partial s}\right)_p \nabla\tilde{s} + \left(\frac{\partial T}{\partial p}\right)_s \nabla\tilde{p} = \frac{1}{\tilde{\rho}}\left(\frac{\partial\rho}{\partial s}\right)_p \nabla\Phi = -\alpha_s\nabla\Phi, \tag{10}$$

which can be used on the right hand side of (8) to give a buoyancy term of the form $-\nabla\tilde{T}s'$.

With the anelastic approximation the continuity equation takes the form

$$\nabla \cdot (\tilde{\boldsymbol{\rho}}\boldsymbol{u}) = 0, \tag{11}$$

thus assuming density fluctuation are small compared to the radially varying mean and eliminating sound waves. This form however allows accounting for the mean variation in density, which for Jupiter and Saturn spans four orders of magnitudes from the cloud level to the bottom of the molecular fluid. Using the anelastic approximation for an isentropic basic state yields a thermodynamic equation

$$\frac{\partial s'}{\partial t} + \frac{1}{\tilde{\rho}}\nabla\cdot(\tilde{\rho}\mathbf{u}s') - \frac{1}{\tilde{\rho}}\nabla\cdot(\tilde{\rho}\boldsymbol{\kappa}\nabla s') = \frac{Q}{\tilde{T}}, \tag{12}$$

where Q is the heating rate per unit mass, and κ is the eddy thermal diffusivity which parametrizes small scale turbulent processes. Then the system (5), (11), (12) can be closed using an equation of state relating density, pressure and entropy fluctuations. In the next section we discuss applying this system to a general circulation model and the details of the equation of state.

3. A deep anelastic general circulation model

We have modified the state-of-the-art MITgcm (Marshall et al., 1997; Adcroft et al., 2007) designed for the dynamics of oceans and atmospheres, and adapted it to giant planets. We have augmented the nonhydrostatic version so that the grid can reach deep into the planet's interior, including the strong variations in gravity and

equation of state. This extension allows the GCM to treat the complete dynamics of a whole sphere of gas instead of just a spherical shell. There is great uncertainty regarding the vertical extent of the dynamical region within the planets interior. Most previous studies have treated a shallower region than we have done here (e.g. Sun et al., 1993; Heimpel et al., 2005). However, it has not been clear how much that choice influences the results (in particular the meridional extent of the superrotation). One of the goals of this work is to study the influence of compressible effects decoupled from influence of the bottom boundary, and therefore we deliberately push the bottom boundary deep even beyond what is generally accepted for giant planets. In Kaspi (2008) we study the dependence of the dynamics on the location of the bottom boundary. As discussed in the introduction, MHD effects, which we do not include here, might put additional limitations on the dynamics (Liu et al., 2007). However, the emphasis here is to study the effects of compressibility on the deep dynamics even without the additional MHD effects.

Traditionally in atmospheric models, the compressible gas is treated by using pressure coordinates as the vertical coordinates, which makes the treatment essentially equivalent to a Boussinesq fluid (Holton, 1992). However, working in pressure coordinates in a nonhydrostatic model brings additional difficulties. To allow the model to be both nonhydrostatic (which is necessary since we wish to study convection and because the Coriolis terms in the vertical momentum equation are not small) and compressible, we include these effects by applying the anelastic approximation, thereby keeping the major effects of the density variation in the mass equation (11).

The anelastic system of Eqs. (5), (11), (12) is solved for the velocity, density, pressure and entropy. To close the system we use an equation of state suitable for high pressure hydrogen as given by Saumon et al. (1995). This equation of state accounts for the variation of the gas properties ranging from close to an ideal gas in the upper levels, to a dense plasma in the interior. The details of the equation of state and its application to the model are given in the section below.

3.1. The equation of state and reference state

The gas is primarily composed of hydrogen and helium with small amounts of heavier elements. At low temperatures and pressures in the outer regions of the planet, hydrogen is a molecular gas and the equation of state may be approximated as an ideal gas. Deeper into the interior, however, due to the high densities and relatively low temperatures (compared to stars), the giant planets lie in an extremely complex thermodynamic regime. The main factors that separate the gas under these conditions from ideal gas behavior are pressure ionization, electron degeneracy, and Coulomb interactions (Guillot, 2005). We use the SCVH equation of state (Saumon et al., 1995), calculated specifically for high pressure hydrogen, including these thermodynamic complexities. The pressure-temperature-density relationship for hydrogen is shown in Fig. 1, where it can be seen that up to about 1 kbar (less than 1% of the radius of Jupiter) the SCVH equation of state is close to an ideal gas, but it differs substantially for the interior.

As discussed in Section 2, using an adiabatic reference state allows the anelastic system to be energetically consistent. This does not limit the form of the equation of state and, for a convective driven interior, is therefore a reasonable approximation (Kaspi, 2008). The *Galileo* entry probe has found the atmosphere to be close to a dry adiabat deeper than the 1 bar level (Seiff et al., 1997). We find that, when taking this value of entropy from the Galileo probe measurement and using it as the adiabat with the SCVH equation of state, the adiabatic profile matches well previous estimates of the interior mean density–temperature–pressure

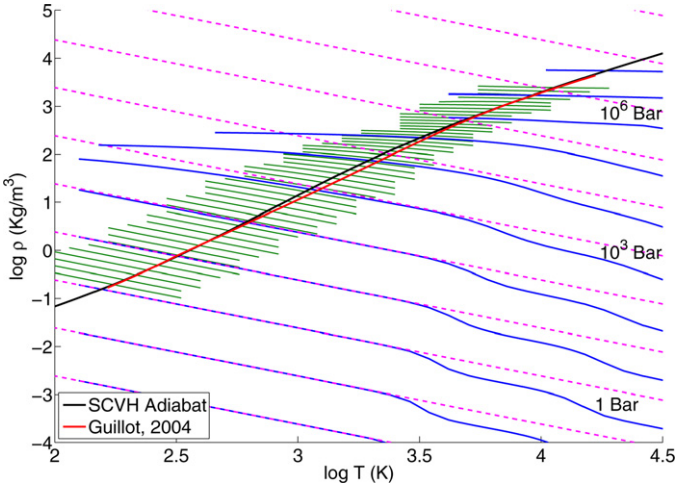

Fig. 1. Contours of pressure in $\log\rho - \log T$ space for the SCVH equation of state (blue) and an ideal gas (magenta). The adiabatic reference state (black) is close to the calculations (red) of Guillot and Morel (1995) and Guillot et al. (2004). The model uses a different polynomial for each layer (green) to calculate the dynamical density (14). (For interpretation of the references to color in this figure legend, the reader is referred to the web version of this article.)

profile (Guillot and Morel, 1995). We therefore use this "Galileo adiabat" as our reference state for the model. The variation from this reference entropy is computed dynamically.

The vertical grid is chosen so that grid spacing follows a constant mean pressure ratio between levels. Relating each pressure level to its vertical depth is set following calculations of Guillot and Morel (1995), and Guillot et al. (2004). Once the constant entropy ($\tilde{s}$), and the mean reference pressure for every vertical grid point are set, the reference temperature and density can be found from the SCVH equation of state. Integrating the reference density allows calculating the gravitational acceleration at every vertical grid point by

$$g(r) = \frac{4\pi G}{r^2}\int_0^r \tilde{\rho}(r')r'^2\,dr', \tag{13}$$

where G is the Cavendish constant, so that the gravitational acceleration is also a function of depth. Note that for Jupiter parameters this radial dependence leads to a maximum in $g(r)$ within the interior of the planet. Fig. 2 shows these reference fields as a function of depth. For the dynamics only $\tilde{\rho}(r)$ and $g(r)$ come in, where the $\tilde{T}(r)$ is used only in the calculation of the forcing profile (see Section 3.2). For every vertical level separately we then fit a polynomial to the SCVH equation of state for the variation in density so that

$$\rho(s,p) = \tilde{\rho} + \left(\frac{\partial\rho}{\partial s}\right)_p s' + \left(\frac{\partial\rho}{\partial p}\right)_s p', \tag{14}$$

where the derivatives are calculated from the SCVH polynomial for each reference pressure, and s' and p' come dynamically from the model equations. This variation in density feeds back to the model dynamics, and thus we have a fully coupled fluid dynamic-thermodynamic system. The modification of the density–pressure–temperature–entropy relationship is a considerable improvement to the existing dynamical models, and gives a much better representation of the planet's interior and its interactions with the outer atmosphere.

3.2. Forcing

Jupiter and Saturn emit more energy than they receive from the sun (Hanel et al., 1981, 1983), and therefore internal heat is

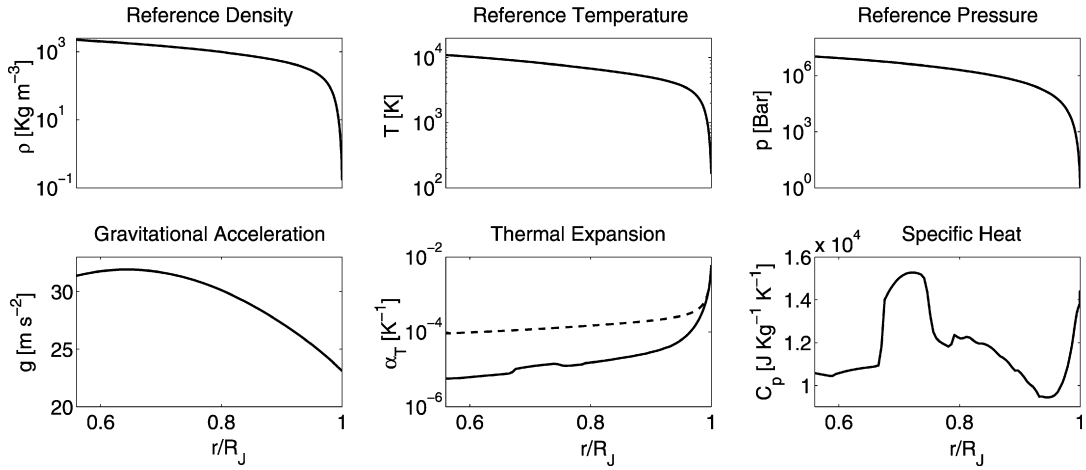

Fig. 2. The adiabatic reference state of the model: Plots of density ($\tilde{\rho}$), temperature ($\tilde{T}$), pressure ($\tilde{p}$), gravitational acceleration (g), thermal expansion (α_T), and specific heat (C_p) as a function of depth. Depth is normalized to the planetary radius (r/R_J). The dashed line in the thermal expansion plot is the value for ideal gas ($1/\tilde{T}$).

transported from the planet's interior to space. The structure of the planet is related to the mechanisms transporting the heat; it is estimated that convection is responsible for most of the heat transport on the giant planets (Guillot et al., 2004). Since we are resolving (albeit coarsely) the convection, the heating term in Eq. (12) is that arising from the divergence of the nonconvective heat fluxes—conductive and radiative.

The entropy of the planet is decreasing at all depths as the gas contracts; the driving for the convection arises when this cooling occurs more rapidly at the surface than at depth. We can equate the global average cooling to a very slow decrease in $\tilde{s}$

$$\frac{\partial \tilde{s}}{\partial t} = \left\langle \frac{Q_{\text{total}}}{\tilde{T}} \right\rangle, \tag{15}$$

where $\tilde{T}$ is the vertical temperature profile calculated from the equation of state, and the brackets represent a density-weighted volume average defined as

$$\langle \cdot \rangle = \frac{1}{\int \tilde{\rho} r^2 \, dr} \int (\cdot) \tilde{\rho} r^2 \, dr. \tag{16}$$

The $Q/\tilde{T}$ term in Eq. (12) represents the deviation from this average $Q_{\text{total}}/\tilde{T} - \langle Q_{\text{total}}/\tilde{T} \rangle$. Thus we have constrained the heating so that, when integrated over the whole mass of the model, the total forcing will be zero, and no net heat is added (or lost) from the system at every time step.

We assume that the transport of heat is diffusive (Kippenhahn and Weigert, 1990) so the heating has the form

$$Q = \eta C_v \kappa \nabla^2 \tilde{T}, \tag{17}$$

where C_v is the specific heat for constant volume, η is a value that sets the magnitude of the heating and is set by the Rayleigh number, and for simplicity we use the same conductivity used for the entropy equation (κ), and represents the combined effects of radiative transfer, conduction, and sub-grid scale motions (which may include small-scale convection). To ensure no net heat gain or loss for s', we shift the profile to give the heating associated with the long time scale cooling. Then the thermodynamic equation (12) including the explicit forcing becomes

$$\frac{\partial s'}{\partial t} + \frac{1}{\tilde{\rho}} \nabla \cdot (\tilde{\rho} \mathbf{u} s') - \kappa \nabla^2 s' = \eta C_v \kappa \left(\frac{\nabla^2 \tilde{T}}{\tilde{T}} - \left\langle \frac{\nabla^2 \tilde{T}}{\tilde{T}} \right\rangle \right). \tag{18}$$

The vertical profile of the heating rate as given by the right hand side of (18), calculated using the $\tilde{T}(r)$ profile, is shown in Fig. 3. The entropy flux (F) is related to the heating rate by $\frac{Q}{\tilde{T}} = \frac{1}{\tilde{\rho}} \nabla \cdot F$. Hence, we can calculate the effective flux at each depth from the heating by

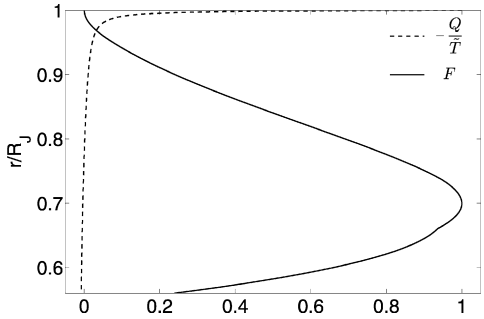

Fig. 3. The prescribed heating profile (dashed) and the resulting heat flux (solid) as a function of depth (normalized to the planetary radius). Both profiles are normalized (note that the heating is negative $(-Q/\tilde{T})$ so that the top levels are effectively cooling and the bottom ones are heating). The integrated mass weighted heating is zero resulting in the flux out of the top level being zero (19).

$$F = \frac{1}{r^2} \int \frac{\tilde{\rho} Q}{\tilde{T}} r'^2 \, dr' + F_0, \tag{19}$$

where F_0 is zero since the flux at the bottom is zero. The normalized heating rate and heat flux are shown in Fig. 3. Note that the flux out of the atmosphere is effectively zero, which is different from Rayleigh–Benard type convection models, that effectively have large outgoing heat fluxes. The interior heat fluxes are very large but compensate for the use of large eddy viscosity terms which are big due to grid size computational limitations. We discuss this issue more in Section 6. We find the model not to be very sensitive to the specific vertical profile of the forcing. To be consistent with the formalism of the MITgcm we define entropy in terms of potential temperature in reference to a reference level. The choice of this level does not affect the dynamics but sets the value of this revised entropy and sets our entropy in units of potential temperature (Kaspi, 2008).

3.3. Model summary

The model solves the full 3D spherical momentum equations with no thin-spherical shell approximations. The mass equation contains compressibility effects, with the mean density varying radially. The thermodynamic equation is expressed in terms of entropy and contains both advection and diffusion of entropy. The equation of state for the variation in density includes both entropy and pressure fluctuations, and the vertically dependent coefficients

are given by the SCVH equation of state. This forms a system of six equations (5), (11), (12) and (14) solved for the six unknowns u, v, w, s', ρ', and p'. The gravitational acceleration $g(r)$ is calculated from the mean density (13). To keep the parameter range simple, and since the grid spacing is fairly uniform (horizontal scales are similar to vertical scales), we use the same viscosity and diffusivity parameters in all the equations. Therefore given the planet's rotation period, the only free parameters are the viscosity (ν), diffusivity (κ) and the magnitude of the forcing (η). These parameters are set by three nondimensional numbers which control the system; the Prandtl (viscosity vs. conductivity), Ekman (viscous damping vs. rotation) and Rayleigh number (heat flux vs. viscous and thermal damping). These numbers are given by

$$Pr = \frac{\nu}{\kappa}, \qquad Ek = \frac{\nu}{\Omega H^2}, \qquad Ra_F = \frac{\alpha_T g F H^4}{C_p \tilde{\rho} \nu \kappa^2}, \tag{20}$$

where H is the total vertical extent of the model, α_T is the thermal expansion coefficient, and F is the flux given by Eq. (19). Note that unlike the Rayleigh–Benard type Rayleigh number, this Rayleigh number (Ra_F) is given in terms of the heat flux and not the temperature contrast between the boundaries, and therefore more appropriate for this model. Since α_T, g, C_p, $\tilde{\rho}$ and F are all varying radially we define the effective Rayleigh number as a the mass averaged value of these properties

$$Ra_F = \frac{H^4}{\nu \kappa^2} \left\langle \frac{\alpha_T g F}{\tilde{\rho} C_p} \right\rangle, \tag{21}$$

where the mass average $\langle \cdot \rangle$ is defined in Eq. (16). Equations (5), (11), (12) can be written in terms of these nondimensional numbers. A useful measure, which was introduced by Christensen (2002), for the Boussinesq case, is the modified Rayleigh number $Ra_F^* = Ra_F Ek^3 Pr^{-2}$ which eliminates the dependence on viscosity and thermal diffusivity, and therefore is a measure of solely forcing and rotation period. For the anelastic case we define this value as

$$Ra_F^* = \frac{1}{\Omega^3 H^2} \left\langle \frac{\alpha_T g F}{\tilde{\rho} C_p} \right\rangle. \tag{22}$$

In the limit of constant properties within the integral in Eq. (22) the modified Rayleigh number coincides with that of Christensen (2002). We note that although adopting this terminology this parameter is essentially different from a Rayleigh number which relates a buoyancy time scale to a diffusive and a viscous time scale, while this modified Rayleigh number relates the buoyancy time scale and the rotation time scale.

For this study we use a horizontal model resolution of 1° in both latitude and longitude, and 120 vertical levels extending to 0.55 of the radius of the planet. The vertical extent corresponds to a pressure variation ranging between 1 bar in the upper level to 12 Mbars in the interior with a constant pressure increase between vertical levels, resulting in an increasingly coarser grid toward the interior. As mentioned before the choice of the relatively deep bottom boundary was chosen in attempt to decouple the dynamics in the upper levels from the choice of the bottom boundary. In Kaspi (2008) we vary the aspect ratio between the inner and outer shell from 0.9 to 0.07 and study the effect of the location of the bottom boundary on the dynamics. The latitudinal extension of the results shown here is from 80° N to 80° S, thus excluding the poles due to numerical limitations. For the analysis presented here we have used both a full longitudinal spherical extent of 360° and a quarter-sphere configuration of 90°. The quarter-sphere configuration is chosen for numerical convenience and is compared to the full sphere configuration in Kaspi (2008), as well as cases with different horizontal and vertical resolution. None of these choices effect qualitatively the results. Slip boundary conditions have been applied to both the bottom and meridional boundaries and a free surface is applied to the upper boundary (Campin et al., 2004). There is no heat flux through the boundaries as shown in Fig. 3. We use Jupiter values for all parameters, including the reference state and the equation of state as discussed in Section 3.1. All results presented here are from instantaneous temporal snapshots of the model after reaching a statistical steady state.

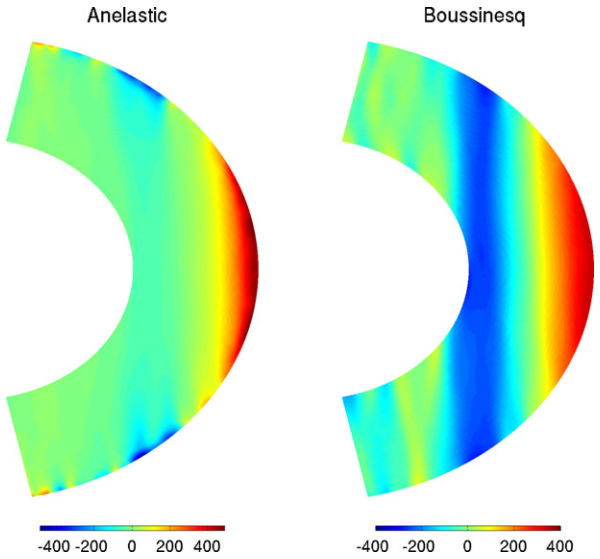

Fig. 4. The zonally averaged zonal velocity ($m\,s^{-1}$) for an anelastic run (left) and a Boussinesq run (right). Runs differ in Rayleigh number: $Ra_F = 3 \times 10^8$ for anelastic and 1×10^9 for Boussinesq. Ekman and Prandtl numbers are equal in both runs: $Ek = 1.5 \times 10^{-4}$ and $Pr = 10$.

4. Numerical results

4.1. The zonal velocity structure: Anelastic vs. Boussinesq

We begin by looking at the zonal wind structure in steady state. To better understand the effect of compressibility and to better compare to previous Boussinesq results (e.g. Heimpel and Aurnou, 2007) we begin by comparing the zonal velocity structure in two similar runs, one anelastic and one Boussinesq. The anelastic case has the density varying by four orders of magnitude from the top level (0.15 $kg\,m^{-3}$) to the interior (2264 $kg\,m^{-3}$) as shown in Fig. 2, while the Boussinesq case is set so that the mean density is constant and equal to the weighted averaged density of the anelastic case (921 $kg\,m^{-3}$). Fig. 4 shows the zonally averaged zonal velocity at statistically steady state for a case where the anelastic and Boussinesq experiments have similar magnitudes of their zonal velocity. Both cases are 1 degree resolution runs with 120 vertical levels, and similar geometry and forcing. For the Boussinesq runs since the mean density does not depend on pressure, the density anomaly (7) is just a function of entropy and not of pressure.

Both runs have a similar velocity structure at the surface; however while the Boussinesq run is barotropic (in the direction of the axis of rotation—z) with strong velocities in the interior, the anelastic case is baroclinic near the surface with strong shears, in the direction of the axis of rotation, at middle and high latitudes with a weaker baroclinic structure (though still not barotropic) closer to the equator. The Boussinesq velocity structure is similar to that seen in previous Boussinesq convection models (e.g. Christensen, 2002). The meridional extent of the superrotation is similar in both cases, and is wider than the superrotating jet on Jupiter. However we find that for a sufficiently shallow system, when the bottom boundary of the model is closer to the upper

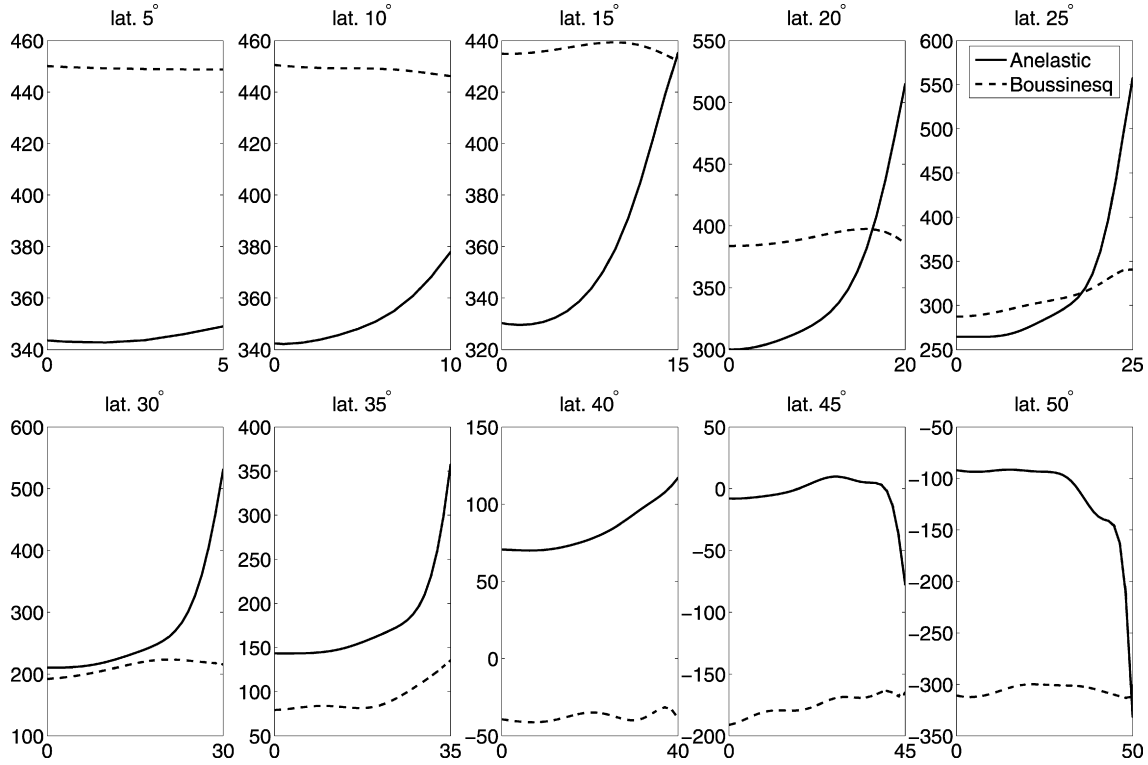

Fig. 5. Zonally averaged zonal velocity for anelastic (full) and Boussinesq (dashed) runs along slices parallel to the axis of rotation. Each slice goes from the upper surface (denoted by the latitude where the slice intersects the upper surface) to the equatorial plane. Slices are separated in 5° in the latitude where they intersect the upper surface. Vertical axis is the zonal velocities ($\mathrm{m\,s^{-1}}$) and horizontal axis is the distance along the slice parallel to the rotation axis (in degrees). Both runs have similar control parameters: $Ra_F = 1 \times 10^9$, $Ek = 1.5 \times 10^{-4}$ and $Pr = 10$. These profiles show the shear resulting from compressible effects (Section 4.4) in the anelastic case verses the Boussinesq case which is more barotropic.

surface, the meridional extent of the superrotation is smaller. Comparing to the width of the superrotation on Jupiter, may imply on the depth on the zonal flow as suggested by Heimpel and Aurnou (2007). In Kaspi (2008) we compare the width of the superrotating jet for different parameter values including the aspect ratio of the inner and outer shell showing this dependence. For the purpose of this study, focusing on the baroclinic wind structure, we will keep the bottom boundary deep. We also note that since the jets are wide the barotropic stability criterion is not violated as observed on Jupiter (Ingersoll and Pollard, 1982). Baroclinic processes caused by meridionally varying solar forcing (emitted from this version of the model) can create sharper jets and violation of the barotropic stability criterion (Kaspi and Flierl, 2007).

To look at the baroclinic structure along the z-axis more specifically we look at the zonal velocity along sections parallel to the direction of the rotation axis for Boussinesq and anelastic runs with similar Rayleigh numbers. In Fig. 5 each zonal velocity section extends parallel to the axis of rotation from the surface to the equatorial plane, and is denoted by the latitude in which it intersects the surface. It shows the wind shear and the much more baroclinic structure in the anelastic case, though interior velocities do not vanish. In the following sections we focus on understanding the structure of the zonal wind for both cases.

4.2. Basic balances

We now turn to a mechanistic understanding of the wind structure. Considering the momentum equation for a rotating fluid (5) we note that in the deep system, a priori all four Coriolis terms contribute to the balance. Typically in oceanic and atmospheric applications (Pedlosky, 1987), since the motion is confined to a thin spherical shell, some of the Coriolis and metric terms can be neglected. However, when studying the dynamics of a full sphere, these terms are not small. In a shallow system, due to the small aspect ratio between vertical and horizontal lengths, the Coriolis term associated with the vertical velocity in the horizontal momentum equation, and the Coriolis term associated with the zonal velocity in the vertical momentum equation are typically neglected. This leads the vertical momentum equation, for small Rossby numbers, to be to the leading order hydrostatic (beyond the hydrostatic basic state). We emphasize that we do not make any of these approximations in our numerical model, and the importance of these typically neglected terms is discussed further below. Similarly in the deep system where r varies considerably, the metric terms maybe important for higher orders. We begin by looking at the leading order balances in statistical steady state. These balances are important for understanding the key physical mechanisms in the dynamics, and for further analysis when developing theories with higher order expansions. Therefore beginning with the zonal momentum balance, for small Rossby and Ekman numbers the leading order terms in the momentum equations (5), (8) in spherical coordinates give

$$-2\Omega \sin\theta v + 2\Omega \cos\theta w = -\frac{1}{\tilde{\rho} r \cos\theta}\frac{\partial p'}{\partial \phi}, \tag{23}$$

$$2\Omega \sin\theta u = -\frac{1}{\tilde{\rho} r}\frac{\partial p'}{\partial \theta}, \tag{24}$$

$$-2\Omega \cos\theta u = -\frac{1}{\tilde{\rho}}\frac{\partial p'}{\partial r} - \frac{\rho'}{\tilde{\rho}} g = -\frac{\partial P'}{\partial r} + \alpha_s g s', \tag{25}$$

where all variables have been defined previously in Section 2. Density and pressure have been expanded as in Eqs. (3), (4) to a mean horizontally independent hydrostatic part and an anomaly, and all four Coriolis terms appear in the leading order balance.

We demonstrate these balances numerically below. In Fig. 6 we show that to the first order with Jupiter parameters the zonal flow is in geostrophic balance; thus (24) holds. In Eq. (23) the zonally averaged Coriolis terms balance each other. The ageostrophic contributions to the meridional momentum equation are an order of magnitude smaller and are dominated by the convection, which gives the signature of plumes aligned with the axis of rotation. This implies that for the parameter regime of Jupiter the assumption of a small Rossby number, which will be used in later analysis, is valid. In the deep spherical shell much of the intuition such as the vertical momentum balance being close to hydrostatic, or the similar scaling of zonal and meridional motions do not hold. In fact, as seen when zonally averaging equation (23), the vertical and meridional velocities tend to be closely linked. The numerical results presented here have Rayleigh, Ekman and Prandtl numbers as defined in Eq. (20), and are 1×10^9, 1.5×10^{-4} and 10 and respectively. The choice of high Rayleigh and Prandtl numbers and a low Ekman number is to make the flow as turbulent as possible. When experimenting with the parameters the results do not change qualitatively (Kaspi, 2008), and the relation to the parameter regime of the giant planets is discussed further in Section 6.

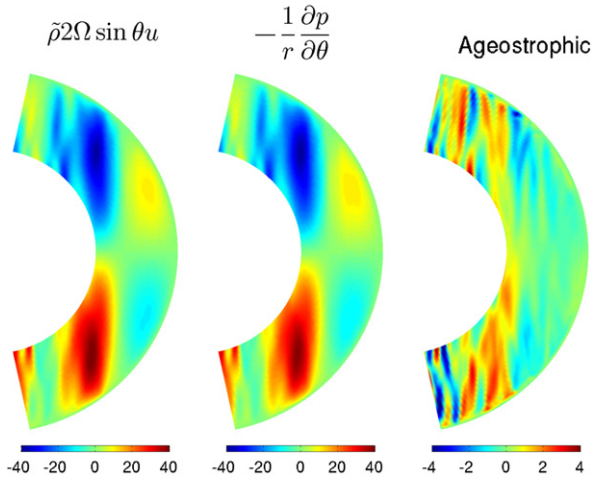

Fig. 6. Geostrophic balance: the two plots on the left show the geostrophic balance (Eq. (24)) for the zonally averaged fields on meridional sections (latitude–radius). The difference between the two left panels (ageostrophic) is shown in the right panel. Model parameters for this example are $Ra_F=1\times10^9$, $Ek=1.5\times10^{-4}$ and $Pr=10$, and units are $\mathrm{kg\,s^{-2}\,m^{-2}}$. Note that color scale is different between the geostrophic and ageostrophic terms, showing the dominance of the geostrophic balance.

Next we look at the vertical momentum balance. In the traditional shallow type system the leading order balance would be between the vertical pressure gradient and buoyancy giving hydrostatic balance (beyond the higher order basic state hydrostatic balance in Eq. (2)). However due to the large aspect ratio, the Coriolis acceleration in the vertical momentum balance is not negligible. In Fig. 7 we show that the difference between the hydrostatic terms is almost exactly the vertical momentum equation Coriolis term. This verifies that Eq. (25) is indeed the leading order balance. This is important when looking at thermal wind balance for the deep system which we do in Section 4.3. Therefore we refer to the basic balance being geostrophic and hydrostatic, but unlike the classic shallow fluid case it includes the nonnegligible vertical Coriolis term.

4.3. Thermal wind balance for the deep anelastic system

Next we revisit the thermal wind relation for a deep atmosphere. As discussed in Section 4.2 the aspect ratio between vertical and horizontal scale is not small, and therefore the Coriolis term in the vertical equation and the one associated with vertical motion in the zonal equation are not negligible. We are interested in the effect of the Coriolis terms and the density gradient on the velocity structure. Taking the radial derivative of the meridional momentum equation and using the vertical momentum equation gives

$$\frac{\partial u}{\partial r}=\frac{g}{2\Omega r\tilde{\rho}\sin\theta}\frac{\partial\rho'}{\partial\theta}-\frac{1}{\tilde{\rho}r}\frac{\partial\rho'}{\partial\theta}\cot\theta u-\frac{1}{r}\cot\theta\frac{\partial u}{\partial\theta}-\frac{1}{\tilde{\rho}}\frac{\partial\tilde{\rho}}{\partial r}u. \quad (26)$$

More information would be needed to get independent expressions for the vertical and latitudinal velocity gradients, but noting that the derivative in the direction parallel to the axis of rotation is given by

$$\frac{\partial}{\partial z}=\sin\theta\frac{\partial}{\partial r}+\cos\theta\frac{1}{r}\frac{\partial}{\partial\theta}, \quad (27)$$

allows writing the zonal velocity gradient in the direction parallel to the rotation axis as

$$\frac{\partial u}{\partial z}=\frac{g}{2\Omega r\tilde{\rho}}\frac{\partial\rho'}{\partial\theta}-\frac{u}{\tilde{\rho}r}\cos\theta\frac{\partial\rho'}{\partial\theta}-\frac{1}{\tilde{\rho}}\frac{\partial\tilde{\rho}}{\partial r}u\sin\theta. \quad (28)$$

This expression includes nonorthogonal derivatives, unlike the standard approximation (Pedlosky, 1987) which is sufficient for a

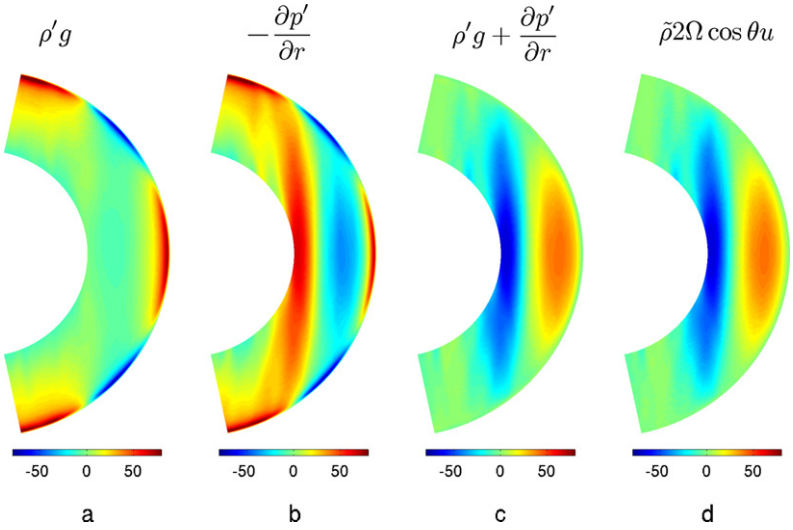

Fig. 7. Hydrostatic balance: (a) $\rho' g$; (b) radial pressure gradient; (c) difference between the two left panels; (d) vertical Coriolis term. Parameters for this example are $Ra_F=1\times10^9$, $Ek=1.5\times10^{-4}$, $Pr=10$, and units are $\mathrm{kg\,s^{-2}\,m^{-2}}$. This points to the importance of the nonhydrostatic Coriolis term in the vertical momentum balance.

shallow system where the shear is associated with the perpendicular density gradient. In addition the zonal velocity gradient has contributions from both the vertical and latitudinal density gradients. Note that all terms on the right hand side have the mean density in the denominator. If density gradients driven by the internal convection have roughly the same scale on the top and bottom of the deep atmosphere, while the density is much bigger at the bottom rather than on top, one may expect a stronger vertical shear on top than at the bottom. Scaling the terms in Eq. (28) shows that the second term on the right hand side is an order $\rho'/\tilde{\rho}$ smaller than the other terms. Then the leading order balance becomes approximately

$$\frac{\partial u}{\partial z} = \frac{g}{2\Omega r\tilde{\rho}}\frac{\partial \rho'}{\partial \theta} - \frac{1}{\tilde{\rho}}\frac{\partial \tilde{\rho}}{\partial r}u\sin\theta. \tag{29}$$

Therefore the shear in the direction of the rotation axis is composed of the meridional density anomaly gradient and the vertical mean density gradient. In Section 4.4 we show numerically how each of these varies spatially.

4.4. The role of compressibility in the baroclinic vorticity production

The balance between the full velocity gradients and the density gradients can be obtained by taking directly the curl of the 3D momentum equation (1), multiplied by the full density ρ giving for small Rossby and Ekman numbers

$$2\Omega\nabla\cdot(\rho\mathbf{u}) - 2\Omega\cdot\nabla(\rho\mathbf{u}) = -\nabla\rho\times\mathbf{g}. \tag{30}$$

Then, assuming the density has a mean horizontally independent hydrostatic part and a smaller anomaly (3), and applying the anelastic approximation (11) gives

$$2\Omega\cdot\nabla(\tilde{\rho}\mathbf{u}) = \nabla\rho'\times\mathbf{g} \tag{31}$$

which is similar to the zonal component of (29). In the Boussinesq limit this gives the standard thermal wind relation. Note that if the right side would vanish this would *not* be the barotropic limit, since in the barotropic limit the cross product of the full density gradient and full pressure gradient vanishes. To see the barotropic limit we rewrite the right hand side of Eq. (31) using (2) as

$$\nabla\rho'\times\mathbf{g} = \frac{1}{\tilde{\rho}}\nabla\tilde{\rho}\times\nabla p' - \frac{1}{\tilde{\rho}}\nabla\rho\times\nabla p, \tag{32}$$

where we have expanded both density and pressure to a hydrostatic part and a smaller anomaly as in Eqs. (3), (4). We have used the fact that the cross product of the mean density and mean pressure gradients is identically zero and dropped higher order terms. In the barotropic limit the second term on the right hand side of Eq. (32) is identically zero, and for a geostrophically balanced fluid the first term would give

$$\begin{aligned}\frac{1}{\tilde{\rho}}\nabla\tilde{\rho}\times\nabla p' &= -\frac{1}{\tilde{\rho}}\nabla\tilde{\rho}\times(\tilde{\rho}2\Omega\times\mathbf{u})\\ &= \mathbf{u}\nabla\tilde{\rho}\cdot 2\Omega - 2\Omega(\nabla\tilde{\rho}\cdot\mathbf{u}).\end{aligned} \tag{33}$$

Using the anelastic approximation and expanding the right hand side of Eq. (30) with (33) gives

$$2\Omega\tilde{\rho}\cdot\nabla\mathbf{u} - 2\Omega\tilde{\rho}\nabla\cdot\mathbf{u} = 0, \tag{34}$$

which is the classic Taylor–Proudman theorem for a barotropic fluid (Pedlosky, 1987). Thus if the fluid is barotropic we would expect that the zonal velocity is independent of the direction parallel to the rotation axis and, if the fluid is also Boussinesq we expect that the full velocity vector is independent of this direction. We are interested though in going away from these two limits and studying the role of the baroclinic effects in an anelastic fluid driven by convection. The convection makes the density gradients nonzero, and the level of baroclinicity will set how far the system is from the Taylor–Proudman regime. The baroclinic form of Eq. (34) can be seen by taking the curl of the momentum equation (1) (without multiplying by the density first). Then for small Rossby and Ekman numbers, and expanding again as in Eqs. (3), (4) gives

$$2\Omega\tilde{\rho}\cdot\nabla\mathbf{u} - 2\Omega\tilde{\rho}\nabla\cdot\mathbf{u} = -\frac{1}{\tilde{\rho}}[\nabla\tilde{\rho}\times\nabla p' + \nabla\rho'\times\nabla\tilde{p}]. \tag{35}$$

Expressing the density in terms of pressure and entropy as in Eq. (6)

$$\nabla\rho'(s,p) = \left(\frac{\partial\rho}{\partial s}\right)_p\nabla s' + \left(\frac{\partial\rho}{\partial p}\right)_s\nabla p', \tag{36}$$

allows rewriting the vorticity equation (35) for an adiabatic reference state to the lowest order as

$$\begin{aligned}2\Omega\tilde{\rho}\cdot\nabla\mathbf{u} - 2\Omega\tilde{\rho}\nabla\cdot\mathbf{u} &= -\frac{1}{\tilde{\rho}}\left(\frac{\partial\rho}{\partial s}\right)_p\nabla s'\times\nabla\tilde{p}\\ &= \left(\frac{\partial\rho}{\partial s}\right)_p\nabla s'\times\mathbf{g}.\end{aligned} \tag{37}$$

Hence, Eqs. (31) and (37) give two equivalent forms of the vorticity equation where the baroclinic terms are given once in terms of the density gradients, and once in terms of the entropy gradients. We have shown in Section 2 that for an anelastic and adiabatic fluid the buoyancy naturally is given in terms of entropy rather than density (since the background density is varying while the entropy is not). Therefore this form of the vorticity equation (37) is consistent with the barotropic limit where the right hand side vanishes. However, while in a Boussinesq fluid the velocity divergence will vanish as well, giving the standard Taylor–Proudman theorem, in the anelastic case it will not and therefore the velocity gradient will depend on the compressibility.

To understand the role of the pressure gradient from Eq. (36) in Eq. (31) we consider only the zonal component of Eqs. (37) and (31), so that

$$2\Omega\frac{\partial u}{\partial z} = -\frac{\alpha_s g}{r}\frac{\partial s'}{\partial\theta}, \tag{38}$$

$$2\Omega\frac{\partial}{\partial z}(\tilde{\rho}u) = -\frac{\alpha_s g\tilde{\rho}}{r}\frac{\partial s'}{\partial\theta} + \frac{\beta g\tilde{\rho}}{r}\frac{\partial p'}{\partial\theta}, \tag{39}$$

where α_s and β are the isentropic and isobaric coefficients defined in Eq. (7). Note that α_s and β depend directly on $1/\tilde{\rho}$ and therefore for the anelastic case can vary considerably with depth. Subtracting Eq. (38) from Eq. (39) shows that the relation

$$2\Omega u\frac{\partial\tilde{\rho}}{\partial z} = \frac{\beta g\tilde{\rho}}{r}\frac{\partial p'}{\partial\theta} \tag{40}$$

must hold. This means that the pressure contribution to the density anomaly accounts for the variation in the mean density. Expression (39) then suggests a few possible situations: if the contribution of Eq. (40) to the right hand side of Eq. (39) is small, then the zonal velocity gradient would depend on the derivative of the entropy anomalies. In the barotropic limit this would give the standard invariance of u in the direction parallel to the axis of rotation, similar to the barotropic Boussinesq case. However if the contribution of Eq. (40) is not small then compressible effects are important. In a particular case where the two terms on the right hand side of Eq. (39) cancel each other then we expect the zonal momentum $(\tilde{\rho}u)$ to be constant along the z axis.

We find that in the statistical steady state of our numerical simulations, the system is in a state in between these two extreme scenarios and that this level of baroclinicity depends greatly on latitude. We find this to be the case consistently for different model parameters and different model resolutions (Kaspi, 2008). In Fig. 8

we look at each of the terms in the vorticity equation to see its relevant contribution in Eq. (39). We can see that the contribution of pressure anomalies to the density anomalies is large especially around the upper boundary, while the entropy contribution is larger in the interior. If we would not have included the pressure variation contribution to density, then the density represented only by entropy anomalies will not be balancing the compressible vorticity production (compressible part of the left hand side of Eq. (39)). In a case of small enough entropy anomalies this will lead to appearance of having $\tilde{\rho}u$ close to constant along the direction of the rotation axis. Therefore we conclude that the pressure contribution to density gradients is crucial when using the anelastic approximation. In a Boussinesq system where the system has a constant mean density the perturbation can be described by only the entropy.

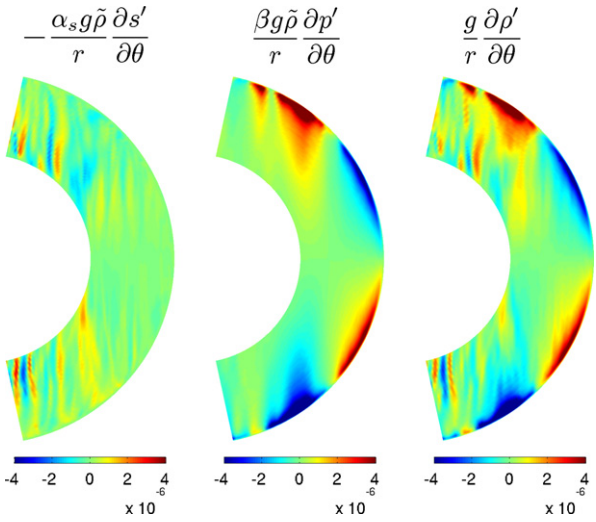

Fig. 8. The contributions of entropy and pressure to the density anomaly and shear. Left: the entropy anomaly contribution to Eq. (39); middle: the pressure anomaly contribution to Eq. (39); right: the density anomaly contribution (equal to the sum of the two left panels: Eq. (36)). Pressure contribution is dominant in the upper levels, and entropy contributions are dominant in the interior. Parameters for this example are $Ra_F = 1\times10^9$, $Ek = 1.5\times10^{-4}$, $Pr = 10$, and units are $\mathrm{kg\,s^{-2}\,m^{-3}}$.

In order to understand the zonal velocity vertical structure we look in Fig. 9 at how the density anomalies discussed above contribute to the shear (through Eqs. (31) and (37)). First we note that looking at the two right panels shows that relation (31) holds as we expect for a small Rossby number. Then breaking this balance into its components on the two left panels shows that at low latitudes the z-shear of the zonal velocity itself is smaller than at high latitudes, but at the higher latitudes where the z-shear of zonal velocity is larger it is accompanied by a compensating shear in $\tilde{\rho}$ leading to a partial cancellation of these two contributions. Therefore due to the effect of compressibility the zonal velocity develops shear along the direction of the axis of rotation.

5. The eddy driven circulation

5.1. Angular momentum balance

In Section 4 we showed that the convectively driven circulation is to the leading order geostrophic and hydrostatic including the full 3D Coriolis vector. We showed these balances for the zonally averaged meridional and vertical momentum balances (Figs. 6 and 7). For the zonally averaged zonal momentum balance this implies that the vertical and horizontal Coriolis terms would nearly balance each other (23). The flow is driven by the dynamical balances and in this section we look at those for the zonally averaged zonal momentum equation. We divide the velocity into a zonal mean and a deviation from that mean denoted by

$$\mathbf{u} = \bar{\mathbf{u}} + \mathbf{u}', \tag{41}$$

where the overbar $\bar{(\cdot)}$ denotes the zonal mean. Then the zonal momentum becomes

$$\frac{\partial\bar{u}}{\partial t} + \frac{\bar{u}\bar{w}}{r} - \frac{\bar{u}\bar{v}}{r}\tan\theta - 2\Omega\sin\theta\bar{v} + 2\Omega\cos\theta\bar{w} + \frac{1}{\tilde{\rho}}\nabla\cdot(\bar{u}\tilde{\rho}\bar{\mathbf{u}}) + \frac{1}{\tilde{\rho}}\nabla\cdot(\overline{\tilde{\rho}u'\mathbf{u}'}) = \nu\nabla^2\bar{u}. \tag{42}$$

Looking at the steady state numerical values in Fig. 10 we find that the lowest order balance is between the two Coriolis terms, the eddy momentum flux divergence and the viscous terms so that

$$-2\Omega\sin\theta\bar{v} + 2\Omega\cos\theta\bar{w} + \frac{1}{\tilde{\rho}}\nabla\cdot(\overline{\tilde{\rho}u'\mathbf{u}'}) \approx \nu\nabla^2\bar{u}. \tag{43}$$

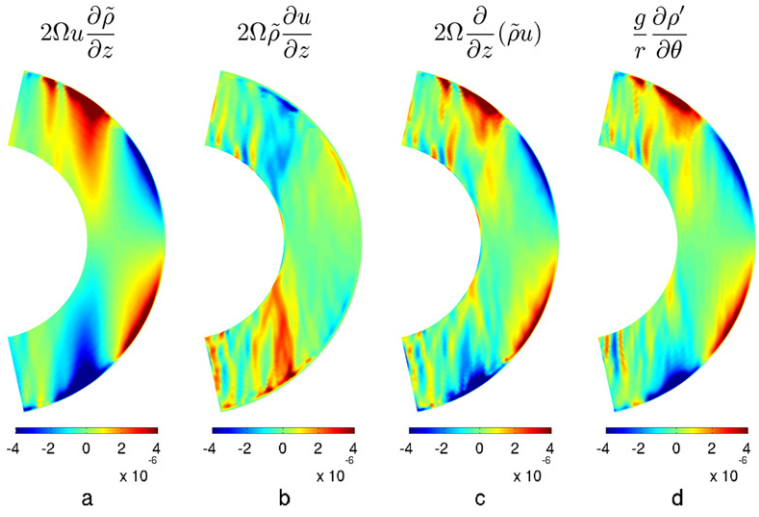

Fig. 9. The vorticity equation balance. The two left panels are the components of the left term in Eq. (39), showing the contributions to the shear in $\tilde{\rho}u$ along the direction of the axis of rotation from the density and velocity gradients separately. Note that these two contributions partially cancel each other as indicated in their sum (c), which is equal to the density anomaly gradient term (d), confirming the balance in Eq. (39) (refer to Fig. 8 for the full balance). The balance in Eq. (40) can be seen by comparing panel (a) to the middle panel in Fig. 8, showing the contribution of the pressure gradients to the vorticity balance in the anelastic system. Near the top the density anomaly is strongly influenced by the pressure anomalies while in the interior density anomalies are influenced by the entropy anomalies. Parameters for this example are $Ra_F = 1\times10^9$, $Ek = 1.5\times10^{-4}$, $Pr = 10$, and units are $\mathrm{kg\,s^{-2}\,m^{-3}}$.

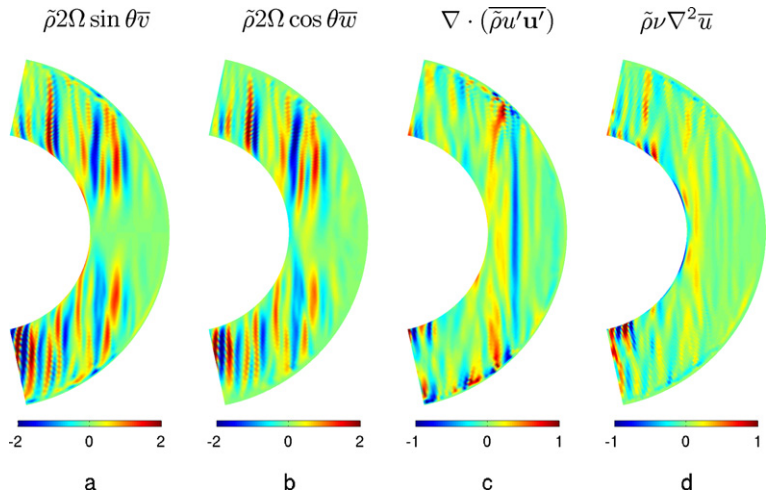

Fig. 10. The zonally average zonal momentum balance leading terms as appear in Eq. (43) (multiplied by $\tilde{\rho}$). Panels (a) and (b) are the two Coriolis terms nearly balancing each other (shown with same sign to better visualize the balance). Panel (c) is the eddy momentum flux divergence and (d) is the viscous momentum flux divergence. Note that since the two right terms have smaller values they have a different color code than the left panels. The small difference between the two Coriolis terms enters the balance between the eddy and viscous flux divergences. Other terms in Eq. (43) have smaller values. Parameters for this example are $Ra_F = 1 \times 10^9$, $Ek = 1.5 \times 10^{-4}$, $Pr = 10$, and units are $\mathrm{kg\,s^{-2}\,m^{-2}}$.

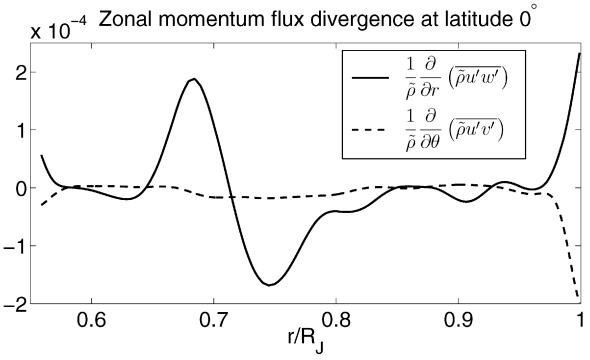

Fig. 11. The radial (solid) and meridional (dashed) contributions to the zonal momentum flux divergence as function of radius (r/R_J) at the equator. This shows the dominance of the radial term on the equator plane (except near the outer boundary where the meridional fluxes converge), and points to the strong eddy momentum flux perpendicular to the rotation axis which is demonstrated in Fig. 12.

In fact, the Coriolis terms dominate the balance nearly balancing each other (as implied by Eq. (23)) and can be considered the leading order balance. Note that in Fig. 10 the eddy momentum flux divergence, and the viscous flux terms have been scaled differently than the Coriolis terms. For simplicity we focus first on the equatorial plane (the equatorial line in the zonally averaged figure). Since the variations along the axis of rotation are small, then the leading order balance on the equatorial plane is

$$\frac{1}{\tilde{\rho}}\frac{\partial}{\partial r}(\overline{\tilde{\rho} w' u'}) \approx \frac{\nu}{r^2}\frac{\partial^2(r^2\overline{u})}{\partial r^2}, \tag{44}$$

where we have kept only the highest order derivatives in the viscosity term, which are dominant. In Fig. 11 we show both components of the momentum flux divergence for a section along the equator. It shows that the momentum flux divergence is dominated by the radial fluxes, except near the outer boundary where meridional fluxes converge. The radial momentum fluxes are outward and big in a localized region. This momentum transfer is the basis for understanding the circulation of the model and the formation of the equatorial superrotation.

It is convenient to rewrite Eq. (42) in terms of the angular momentum

$$M = \Omega r^2 \cos^2\theta + ur\cos\theta, \tag{45}$$

so that Eq. (42) to leading order becomes

$$\frac{\partial \overline{M}}{\partial t} + \frac{1}{\tilde{\rho}}\nabla\cdot(\tilde{\rho}\overline{\mathbf{u}}\overline{M}) + \frac{1}{\tilde{\rho}}\nabla\cdot(\tilde{\rho}\overline{\mathbf{u}'M'}) = \nu\nabla^2\overline{M}, \tag{46}$$

where we have split the angular momentum into a perturbation and a zonal mean. Integrating this equation multiplied by the mean density over a volume contained by the exterior surface and a constant angular momentum surface (which is nearly parallel to the axis of rotation because of the dominance of the solid-body component of M), will cause the contribution from the mean fluxes to vanish since

$$\int \nabla\cdot(\tilde{\rho}\overline{\mathbf{u}}\overline{M})\,dV = \overline{M}\int \nabla\cdot(\tilde{\rho}\overline{\mathbf{u}})\,dV = 0. \tag{47}$$

Therefore in steady state the viscous flux is necessary to balance the angular momentum eddy fluxes. This also shows that for a 2D axisymmetric model there can be no gain of angular momentum (Hide, 1969). Only eddy angular momentum fluxes can carry angular momentum across mean angular momentum contours (although locally mean fluxes can do so as well). Comparing the angular momentum mean fluxes (without the solid body component of M), to the angular momentum eddy fluxes in Fig. 12, we find that while the mean fluxes transfer angular momentum mainly parallel to the mean angular momentum contours, the eddy fluxes transport the angular momentum across mean angular momentum contours to low latitudes. This transfer of angular momentum through the turbulent fluxes to the equatorial outer regions of the planet drives the equatorial surface superrotation. As indicated by Eq. (46) it is the convergence of the flux that causes the superrotation (we discuss this mechanism more in Kaspi, 2008). Boussinesq convection models have shown similar equatorial superrotation at the surface (e.g. Christensen, 2002; Heimpel et al., 2005), while most shallow models have not been able to provide a mechanism for superrotation. However, recently shallow models using bottom drag to parametrize the deep circulation and intrinsic heat fluxes (Schneider and Liu, 2009), or radiative damping (Scott and Polvani, 2008), have been able to show under Jupiter conditions superrotation as well.

The right hand panel of Fig. 12 shows the equivalent eddy heat and mean heat fluxes. As opposed to the angular momentum, there are strong entropy fluxes also in high latitudes. This

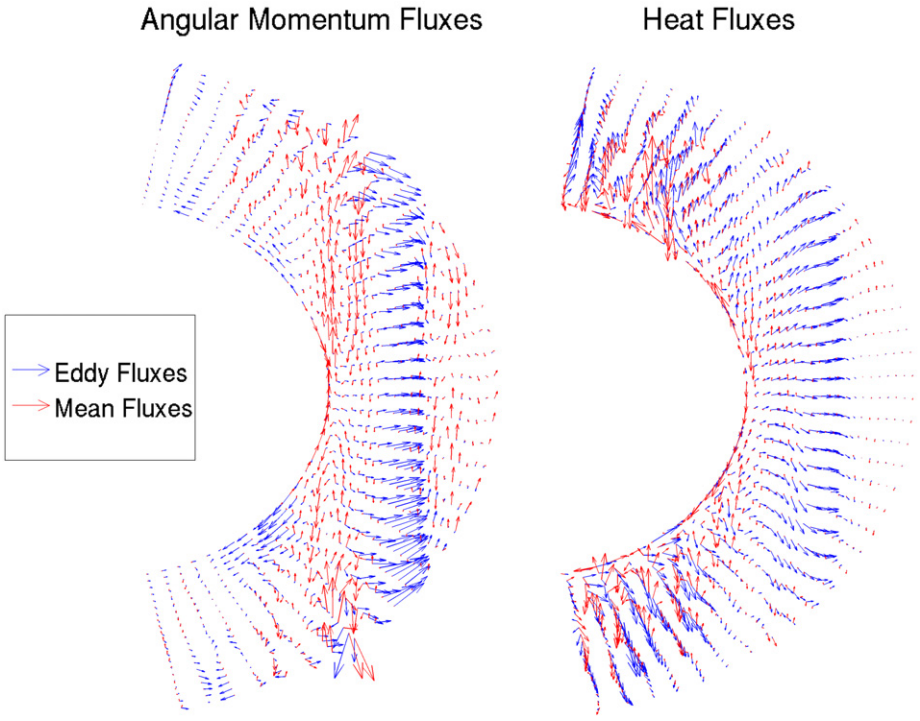

Fig. 12. Zonally averaged angular momentum (left) and heat (right) mean (red) and eddy (blue) fluxes in a meridional cross section. Longer arrows indicate larger flux values. This shows the dominance of the eddy angular momentum fluxes in driving the surface superrotation at low latitudes. Parameters for this example are $Ra_F = 1 \times 10^9$, $Ek = 1.5 \times 10^{-4}$, $Pr = 10$. (For interpretation of the references to color in this figure legend, the reader is referred to the web version of this article.)

transfer of heat mainly parallel to the rotation axis moves heat from lower to higher latitudes (a section parallel to the rotation axis intersects the surface at a higher latitude in the outer shell than in the inner shell). This results in heating of the polar regions. It is possible that this mechanism of heat transport to higher latitudes by internal heat fluxes parallel to the axis of rotation can balance the solar heating, resulting in the observed flat emission on Jupiter and Saturn (Ingersoll and Porco, 1978; Aurnou et al., 2008). Fig. 13 shows the zonally averaged surface velocities and normalized mean angular momentum. At low latitudes we find a Hadley cell (weaker than the zonal flow) which

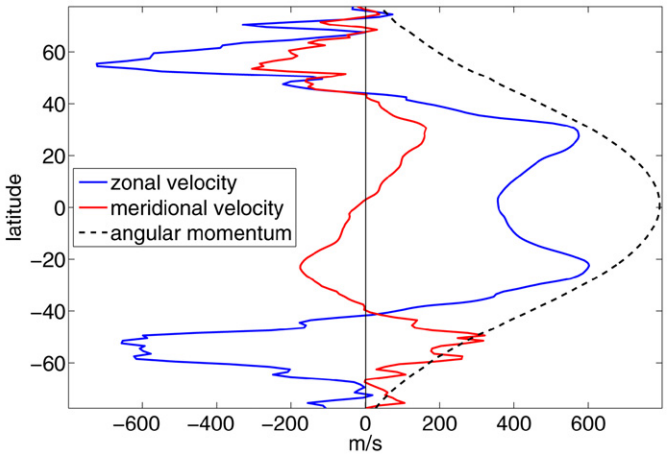

Fig. 13. The zonal (blue), meridional (red) zonally averaged 1 bar surface velocities, and normalized mean angular momentum (dashed black) for a run with parameters: $Ra_F = 1 \times 10^9$, $Ek = 1.5 \times 10^{-4}$ and $Pr = 10$. Surface velocity strength dependence on Rayleigh and Ekman numbers can be inferred from Fig. 19. Vertical structure of the velocity field for these parameters is shown in the left panel of Fig. 17. (For interpretation of the references to color in this figure legend, the reader is referred to the web version of this article.)

is driven by the equatorial fluxes seen in Fig. 12. At high latitudes, exterior to the region of the strong eddy angular momentum flux convergence, we find an inverse meridional cell (surface flow away from the pole), which is a surface return flow driven by the poleward heat flux. The latitude where eddy angular momentum fluxes are zero, meaning that the mean surface zonal velocity is zero, is also where the meridional surface flow vanishes due to the relation between the meridional velocity and the eddy flux divergence (43). The maximum in zonal velocity appears where there is the strongest convergence of angular momentum eddy flux. We note that when the model is shallower the latitudinal width of the superrotating region does depend on the location of the bottom boundary (see examples in Kaspi, 2008), meaning that for a shallower system this whole mechanism will be constrained to a shallower region resulting in a narrower superrotating region, more resembling the jovian observations. The magnitude of the velocity seen in Fig. 13 does depend on Rayleigh number (Fig. 19). Since these simulations do not include solar forcing, there are no implied atmospheric meridional temperature gradients and therefore no upper level baroclinic instability. Such processes could cause formation of multiple zonal jets in the higher latitudes (Kaspi and Flierl, 2007; Schneider and Liu, 2009).

5.2. Formation of columnar convection

We now look at the equatorial plane, thus a slice in radius and longitude along the equator. The most prominent feature, beyond the strong prograde velocities near the upper boundary and the retrograde velocities near the inner boundary (as indicated by Fig. 4), are large positively rotating (with respect to the rotation of the planet) eddies in the interior. Busse (1976) has suggested that Taylor columns can form within a hot convective interior and the interaction of the columns can drive the jets in the atmosphere. Zhang and Schubert (1996) have shown formation of convection

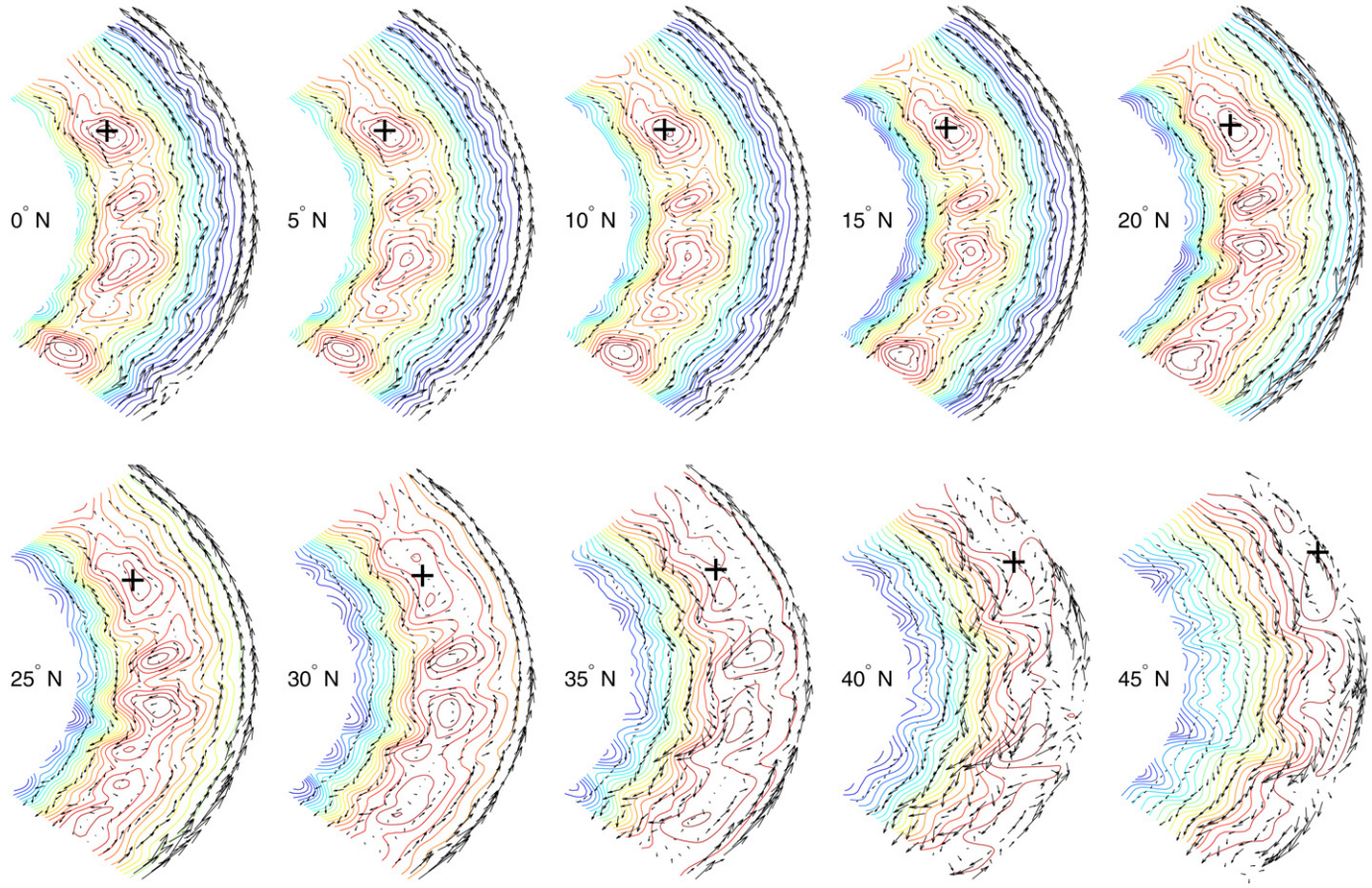

Fig. 14. The 2D streamfunction on slices oriented toward the center of the planet (radius–longitude surfaces), showing the formation of columns which are driven by the convection. Each panel shows a slice tilted in an angle (spread apart by 5° in latitude) going northward from the equator. Red represents cyclonic (anti-clockwise) circulation and blue is anti-cyclonic circulation. The flow is also indicated by the arrows, where longer arrows are stronger velocities. Plus signs are located at an equal distance from the rotation axis in all panels, and located within one of the columns, showing that the eddies seen in the slices are part of columns that are parallel to the axis of rotation. Parameters for this example are $Ra_F = 1 \times 10^9$, $Ek = 1.5 \times 10^{-4}$, $Pr = 10$. (For interpretation of the references to color in this figure legend, the reader is referred to the web version of this article.)

cells in a Boussinesq 3D model for Rayleigh–Benard type convection. Here we use the anelastic model to show the formation of such columnar structures, parallel to the axis of rotation, that extend almost from the surface in one hemisphere to the surface in the other, crossing the equatorial plane at about 2/3 the planetary radius. In Fig. 14 we show the 2D streamfunction on slices along the longitude–radius planes on constant latitude surfaces (so that the surfaces are *not* parallel). The 2D streamfunction is calculated by defining a 3D streamfunction Ψ by

$$\nabla \times \Psi \equiv \tilde{\rho}\mathbf{u}, \tag{48}$$

where we have used the fact that the total momentum is nondivergent (11). Then assuming the variations along the axis of rotation are small we can calculate the meridional component of Ψ by integrating the velocity fields, giving an approximate 2D streamfunction to demonstrate the flow on these surfaces. The slices in Fig. 14 are spread apart by 5° in latitude going northward from the equator. The closed structures on the equatorial plane (upper left panel) extend out in radius as they move out in latitude so that they are parallel to the rotation axis. To demonstrate this we have marked the center of one of the columns on the equatorial plane with a plus sign, and the plus signs on the other planes have an equal distance to the rotation axis, and the same longitudinal angle. We find these columnar features to be a robust feature in all numerical experiments.

5.3. The effect of rotation

We have shown that for the parameter regime of Jupiter and Saturn since Rossby numbers are small, rotation is important in the basic balances and causes motion around columns parallel to the axis of rotation. For the anelastic case, due to having a mean state with a density gradient, the buoyancy frequency is defined in terms of entropy rather than density. We find the buoyancy frequency by differentiating in time the linear nonrotating inviscid case of the vertical momentum equation (8) giving

$$\frac{\partial^2 w}{\partial t^2} - w\frac{\partial s'}{\partial r}\frac{\partial \tilde{T}}{\partial r} = -\frac{\partial^2 P}{\partial r \partial t}, \tag{49}$$

where we have used relations (12) and (10) as well. Therefore for the anelastic system the equivalent to the traditional Brunt–Väisälä frequency is

$$N^2 = -\frac{\partial s'}{\partial r}\frac{\partial \tilde{T}}{\partial r}. \tag{50}$$

Since in Eq. (49) the temperature gradient replaced gravity, and we have shown that entropy rather than density is the natural variable for buoyancy in the anelastic system, then this form of N^2 is the natural outcome. For the convective system however this value becomes either negative if convection is strong, or positive but very small if convection is weak enough and concentrated in plumes. Although in a convective system this is not the oscillation

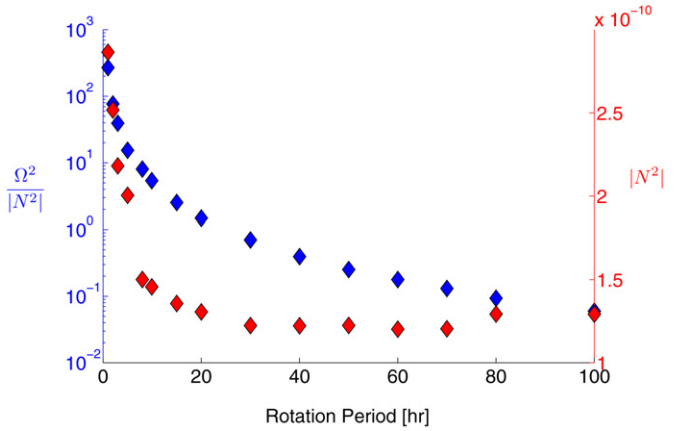

Fig. 15. The ratio $\Omega^2/|N^2|$ (blue) and the value of $|N^2|$ (red, calculated using Eq. (50)) as a function of the rotation period. In all runs the Rayleigh and Prandtl numbers are kept constant ($Ra_F = 3 \times 10^8$, $Pr = 10$), and Ekman numbers vary due to the change in rotation period (viscosity is kept constant). Although the Rayleigh number is kept constant $|N^2|$ does decrease with increasing rotation period. $\Omega^2/|N^2|$ also decreases with increasing rotation period reaching the value of unity (where the character of the flow turns from rotationally to convectively dominated) at a rotation period of roughly 30 hours. This point is close to where the zonal equatorial flow turns from superrotating to subrotating (see Fig. 16). (For interpretation of the references to color in this figure legend, the reader is referred to the web version of this article.)

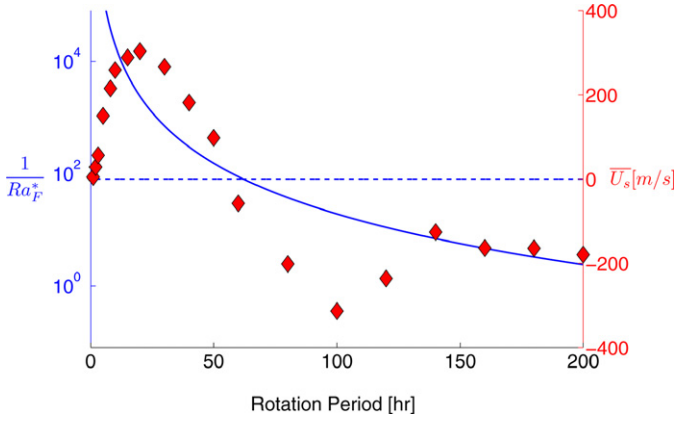

Fig. 16. The zonally averaged equatorial zonal velocity at the 1 bar surface (red) and the modified Rayleigh number $Ra_F^* = Ra_F Ek^3 Pr^{-2}$ (blue) as function of the rotation period, for a set of experiments with equal parameters but varying rotation. In all runs the Rayleigh and Prandtl numbers are kept constant ($Ra_F = 3 \times 10^8$, $Pr = 10$), and Ekman numbers vary due to the change in rotation period (viscosity is kept constant). As the rotation period grows at approximately 50 hours the equatorial zonal velocity switches from flowing east to west. The modified Rayleigh number at this point is 80. Note that different definitions of the modified Rayleigh number (22) can give different critical values, but physically this value is the point where rotation is slow enough so it does not drive convection columns and alignment with the axis of rotation. (For interpretation of the references to color in this figure legend, the reader is referred to the web version of this article.)

frequency due to stratification, the absolute value gives a good dynamical measure for the intensity of the convection. In Fig. 15 we show a set of experiments where we vary the rotation period for a given model configuration. We find that the value of $|N^2|$ grows (even though the Rayleigh number is kept constant) with faster rotation period, and $\Omega^2/|N^2|$ grows too. To a reasonable approximation when $\Omega^2/|N^2|$ is greater than one convection aligns with the axis of rotation, while when $\Omega^2/|N^2|$ is less than one convective plumes go away from the center of gravity and are less influenced by rotation. Therefore this ratio, between the rotation time scale and the buoyancy time scale, gives a good characterization of the flow.

A similar measure describing the ratio between buoyancy flux and rotation that is better defined in terms of convection, and uses the nondimensional parameters of this system, is the modified Rayleigh number discussed in Section 3.3, namely $Ra_F^* = Ra_F Ek^3 Pr^{-2}$. Compared to the Rayleigh number (21) the advantage of this number is that it eliminates the dependence on eddy viscosity and diffusivity. In Fig. 16 we plot the equatorial mean zonal velocity for a set of experiments varying only in rotation period, with the Ra_F^{*-1} value superimposed. We find that for rotation periods smaller than 60 hours (for Jupiter parameters) the equatorial zonal velocity is eastward (superrotating), while for larger rotation periods the equatorial zonal velocity is westward (subrotating). When increasing the rotation period the zonal velocity first increases (peaking at 20 hours), and then decreases until becoming negative for slow rotation. The modified Rayleigh number at the point where the equatorial flow changes from superrotating to subrotating is $Ra_F^* = 1/80$. Thus small modified Rayleigh numbers (big Ra_F^{*-1} in Fig. 16) are dominated by the rotation and indicate superrotation, while when rotation is slow Ra_F^* is large (dominated by the buoyancy flux) and there is no superrotation. Note that the actual value of Ra_F^* where this transition occurs is sensitive to the way the Rayleigh number is defined (Eq. (21)), and to parameters such as the length scale H, and thus we do not expect this value to be necessarily unity at the critical point. However physically this point indicates the transition from rotationally dominated convection where the flow aligns with the rotation axis as discussed in previous sections to where rotation is not dominating the dynamics. At that point the mechanism discussed in Section 5.1 (Fig. 12) breaks since convective columns along the direction of the axis of rotation do not form, and therefore there is no eddy angular momentum flux to the planet's exterior.

We find two very distinct types of flow in the two regimes. The faster rotation experiments all have equatorial superrotation, and interior flow along the axis of rotation with shear in the zonal velocity as discussed in Section 4. Beyond a rotation period of 60 hours however, the nature of the dynamics changes quite rapidly and the zonal mean develops large closed circulations in the radius–latitude plane with no alignment with the rotation axis, and subrotating equatorial zonal velocity. In Fig. 17 we show the zonally averaged velocity for two examples out of this set of runs, one with the rotation period of Jupiter (9.92 hours), and the second with a rotation period of 80 hours. We find one of these two states to appear for the whole range of experiments presented in Figs. 15 and 16. The transition between the two states at a rotation period of 60 h is very rapid. Both the estimate for this transition based on $\Omega^2/N^2 = 1$ and the one based on the value of Ra_F^* are only order of magnitude estimates (since for example for N^2 we are approximating the mean buoyancy in the whole domain), but seem to be a good indicator of the nature of the velocity field.

The subrotating equatorial flow for the slow rotating cases seen in Figs. 15 and 16 might lead to think about the ice-giants, Uranus and Neptune, where the observed equatorial zonal velocities are subrotating. This striking difference between the ice giants and the gas giants has been an issue of ongoing debate. Aurnou et al. (2007) who find similar behavior for the transition between superrotation and subrotation in Boussinesq experiments, suggest that the ice-giants may be in the regime of large Ra_F^* and therefore convectively rather than rotationally dominated. We do not have an equation of state for the interior of the ice-giants which will allow testing this with this model. However based on the gas-giant experiments we find this to be unlikely due to the weak convection on these planets, while rotation rates are 17 and 16 hours on Uranus and Neptune respectively and therefore not slow enough to compensate for the much weaker convection. Therefore for both ice-giants we expect Ra_F^* to be small such that the flow is dominated by rotation. Still, baroclinic effects (Section 4.4) may pre-

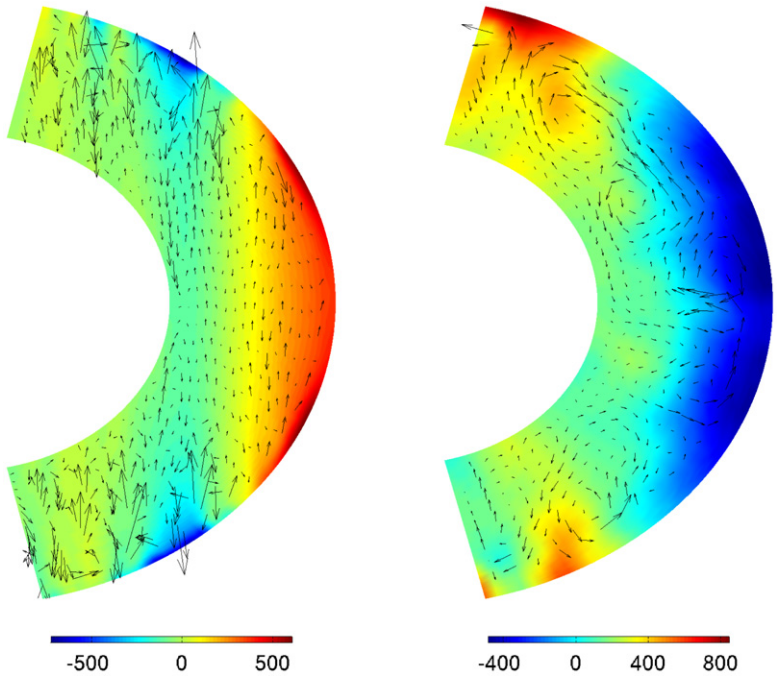

Fig. 17. The effect of rotation: Velocity fields for a fast and slow rotating planet. (Left) rotation period of 9.92 hours; (right) rotation period of 80 hours. In color are the zonal mean zonal velocities where red is eastward, and the arrows are the zonally averaged radial and meridional velocities where longer arrows indicate faster flow. Zonal velocity magnitudes are given in $\mathrm{m\,s^{-1}}$, and interior vertical and meridional velocities indicated by the arrows are two orders of magnitude weaker than the zonal velocities. Ekman numbers are $Ek = 4 \times 10^{-4}$ and $Ek = 3 \times 10^{-3}$ for the fast and slow runs, respectively, and $Ra_F = 3 \times 10^8$, $Pr = 10$ in both runs. (For interpretation of the references to color in this figure legend, the reader is referred to the web version of this article.)

vent the formation of the columns even though the flow is nearly geostrophic, and therefore not drive the outward flux of angular momentum creating the superrotation. Then, the convection along the axis of rotation will cause an equatorial return flow aloft, and therefore transfer lower angular momentum fluid to the equator causing the equatorial subrotation.

6. Scaling and parameter sensitivity analysis

In this section we try to relate the results of the model to the actual physical parameter regime of Jupiter. Although we are using a realistic equation of state and realistic vertical thermodynamic profiles, due to numerical grid-size limitations the numeric viscosities and heat flux are much larger than those of Jupiter. This is a common feature of numerical models where turbulent viscosities and thermal diffusivities represent the average turbulence within a grid box rather than the molecular values. Therefore the Ekman numbers (20) are orders of magnitude too large, and Rayleigh numbers would be very small if not compensated by effectively large heat fluxes. In order to reach Rayleigh numbers which exceed critical and are as turbulent as the numerics allow, the large viscosities and diffusivities are offset by effectively large heat fluxes exceeding the values we believe exist on the giant planets. In fact, even when over-prescribing the forcing, the Rayleigh numbers are many orders of magnitude smaller than the planetary ones using molecular values. This suggests that thinking of these type of models only in terms of the nondimensional parameters, and not in terms of the actual heat fluxes, viscosities, diffusivities, etc., may be more appropriate. Nevertheless, our objective is to infer from these models about actual characteristics of the planet, and overforcing the heat flux is an issue we should address. Therefore in order to show the dependence on the forcing, we present our numerical results for a range of Ekman and Rayleigh numbers, although still being away from real planet values which will require much finer numerical grids that are not achievable with current computational abilities.

We first begin by examining whether the velocities in our model can be estimated by simple convection scaling arguments. Following Fernando et al. (1991), and Ingersoll and Pollard (1982), we estimate the mean heat flux carried by convection as

$$F = \tilde{\rho} C_p w' \Delta T, \tag{51}$$

where ΔT is the typical temperature difference across plumes, and w' is the convectively driven vertical velocity. Due to the rotation we can relate the production of vorticity and the buoyancy anomaly via the vertical momentum balance which gives a balance between the Coriolis force and the buoyancy so that

$$\Omega u' = \alpha_T g \Delta T. \tag{52}$$

Here we assumed that the contributions from pressure and entropy perturbations discussed in Section 4.4, are on average for scaling arguments of equal magnitude. Now using Eqs. (51) and (52) we can write an expression for $\overline{u'w'}$ as a function of the thermodynamic variables and the heat flux so that

$$\overline{u'w'} = \frac{\alpha_T g F}{\tilde{\rho} C_p \Omega}. \tag{53}$$

All variables on the right hand side of Eq. (53) are given by the equation of state and the reference state of the model (Fig. 2). The flux can be inferred from the prescribed radial heating profile (19). Comparing the right hand side term in Eq. (53) shows a good agreement with the eddy rms velocities given by the model; this is shown in Fig. 18. This means that the convectively driven velocities are on average well approximated by these arguments, even though the convective velocities themselves are stronger than what we expect on Jupiter because the heat flux prescribed to the model is stronger than the heat flux we expect to find on Jupiter. Using Jupiter atmospheric values of $F = 6\ \mathrm{W\,m^{-2}}$, $\alpha_T = 10^{-2}\ \mathrm{K^{-1}}$, $C_p = 1.3 \times 10^4\ \mathrm{J\,kg^{-1}\,K^{-1}}$, and $\rho = 0.1\ \mathrm{kg\,m^{-3}}$, and interior values of $\alpha_T = 10^{-5}\ \mathrm{K^{-1}}$, and $\rho = 10^3\ \mathrm{kg\,m^{-3}}$, we find convective velocities on the orders of $1\ \mathrm{m\,s^{-1}}$ at the 1 bar

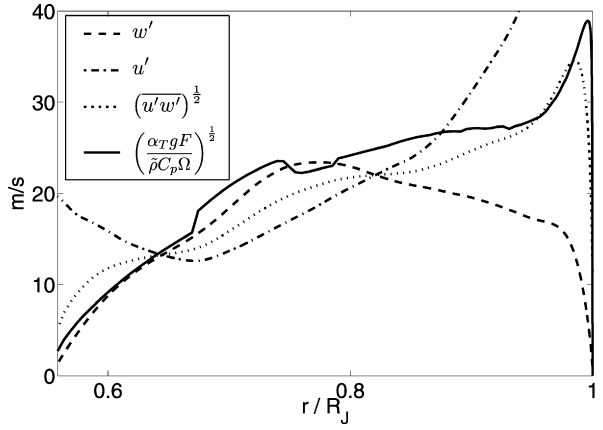

Fig. 18. Scaling for the convective velocities in the model. $\overline{u'w'}$ (solid) is estimated from both scaling given the model thermodynamic properties and the forcing profile (53) (dotted), and from the model rms eddy velocities as a function of depth. The rms eddy velocities u' (dash–dot) and w' (dashed) are shown each independently, where w' is bounded to zero at the upper and lower boundaries while u' has slip boundary conditions. Model parameters for this run are $Ra_F = 1 \times 10^9$, $Ek = 1.5 \times 10^{-4}$, $Pr = 10$, and units are $\mathrm{m\,s^{-1}}$.

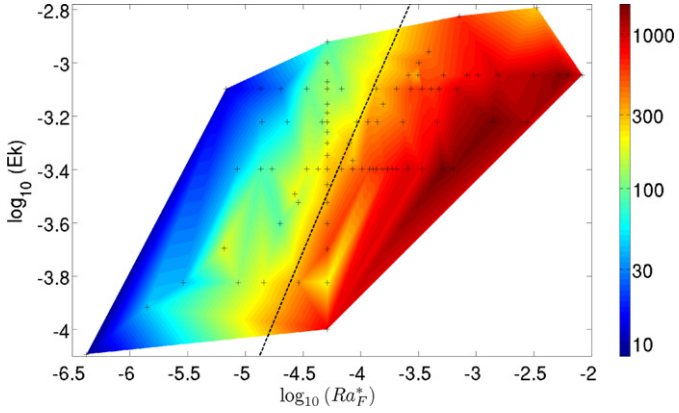

Fig. 19. The magnitude of the equatorial superrotating zonal velocity ($\mathrm{m\,s^{-1}}$) as a function of Ekman number and the modified Rayleigh number (22) for a range of numerical experiments. All runs have a constant rotation period (9.92 hours). The mean slope (dashed) of constant superrotating zonal velocity is $Ra_F^* \cdot Ek^{-5/4} =$ constant, indicating the zonal velocity dependence on both Ekman number (viscosity) and heat flux. The regime of Jupiter will be far to the bottom left corner.

level and 10^{-3} $\mathrm{m\,s^{-1}}$ for the interior. This shows a significant change in the convective velocities between the atmosphere and the interior, and both cases, as shown in Fig. 18, are smaller than model eddy velocities. Nonetheless the model mean velocities associated with zonal winds are of the right order of magnitude, and for small Rossby numbers are geostrophically balanced, therefore the mean densities and thermal wind may be well represented. Bridging this gap between the overforcing and the resulting scales is a major challenge for numerical modeling of convective systems.

To further relate the parameter regime of the model to that of Jupiter, we show in Fig. 19 a set of numerical experiments where we study the dependence of the equatorial superrotating upper surface zonal velocity on both the Ekman number and the modified Rayleigh number (which for a constant rotation period represents the magnitude of the heat flux). The various experiments we use to create this analysis are discussed in further detail in Kaspi (2008), and all have a constant rotation period. If zonal velocities would be independent of the modified Rayleigh numbers for a constant Ekman number then one could infer from the numeric regime to the planet's regime as suggested by Christensen (2002), who assumes the numerical results asymptote to a regime where molecular quantities are not important. However Fig. 19 shows that for experiments with roughly equal superrotation magnitude, the relation between Ekman number and forcing is roughly $Ek^{5/4} \sim Ra_F^*$. This means that if numeric results could be extrapolated to the real planet regime, the effect of the large eddy viscosities should be compensated by a large prescribed heat flux following the slope suggested in Fig. 19. This implies that the Rayleigh number containing the ratio of the heat flux to viscosity and diffusivity might be a good measure for such models, rather than heat flux (or modified Rayleigh number) independently.

The results shown in Fig. 19 show that the magnitudes of the zonal velocities in the model are sensitive to the magnitude of the forcing. However, it is important to note that the vertical profile of the zonal winds does not depend on the forcing or other parameters. Therefore we find that the analysis in Section 4 is robust and invariant of the parameter regime we have been able to explore. To demonstrate this we look at the zonal velocities along sectors parallel to the rotation axis for different Rayleigh number experiments. These are shown in Fig. 20, where the sections are separated by 5° in latitude, and extend from the outer surface to the equatorial plane. The sections are denoted by the latitudes at which the sections intersect the top surface. These sections show that the baroclinic profiles of the velocity (which in Fig. 20 are normalized by the Rayleigh number ratio) are similar for different Rayleigh numbers. The latitudinal differences are due mainly to the variation in density and thermal expansivity which have different profiles along different sections. This shows that although the value of the velocity depends on Rayleigh number the baroclinic profile does not, and therefore the result of weaker zonal velocities in the interior is robust. The vertical profile of zonal velocity is in a state in between the barotropic limit of constant velocity, and momentum column limit of constant momentum discussed in Section 4.3. The variation in the magnitude of the velocity along the axis of rotation is due to the vertical variation in density. The Boussinesq analog of this figure is shown in Fig. 5, and demonstrates this effect.

7. Conclusion

We develop a new general circulation model for the giant planets. The model solves the full 3D, anelastic, nonhydrostatic Navier–Stokes equations on a rotating sphere, extending vertically from the surface to a small interior core. This model is an improvement over previous convection models in several respects including the use of the anelastic approximation, incorporating therefore the vertical density variation within the planet; realistic thermodynamics including an isentropic reference state and the SCVH equation of state; a radially varying gravity field; and a continuous heating forcing profile representing gravitational cooling rather than the simpler Rayleigh–Benard convective forcing. These improvements make the physical interpretation of this model more realistic and applicable to the giant planets. In addition this model is part of the MITgcm standard package, which is open source code available at www.mitgcm.org. The accessibility of this model should allow easier comparisons between different models.

The anelastic approximation allows us to study how compressibility effects affect the convectively driven flow in a rotating system. We find that for the parameter regime of Jupiter and Saturn the interior flow develops alignment with the axis of rotation. However instead of having pure Taylor columns with zonal velocities constant along the axis of rotation as suggested by the Boussinesq models, we find significant baroclinic shear. By studying the vorticity balance we find that the baroclinic vorticity production is not small due to the compressible effect, and this creates the shear along the direction of the rotation axis. Since the shear is associated with compressibility most of the shear is in the outer

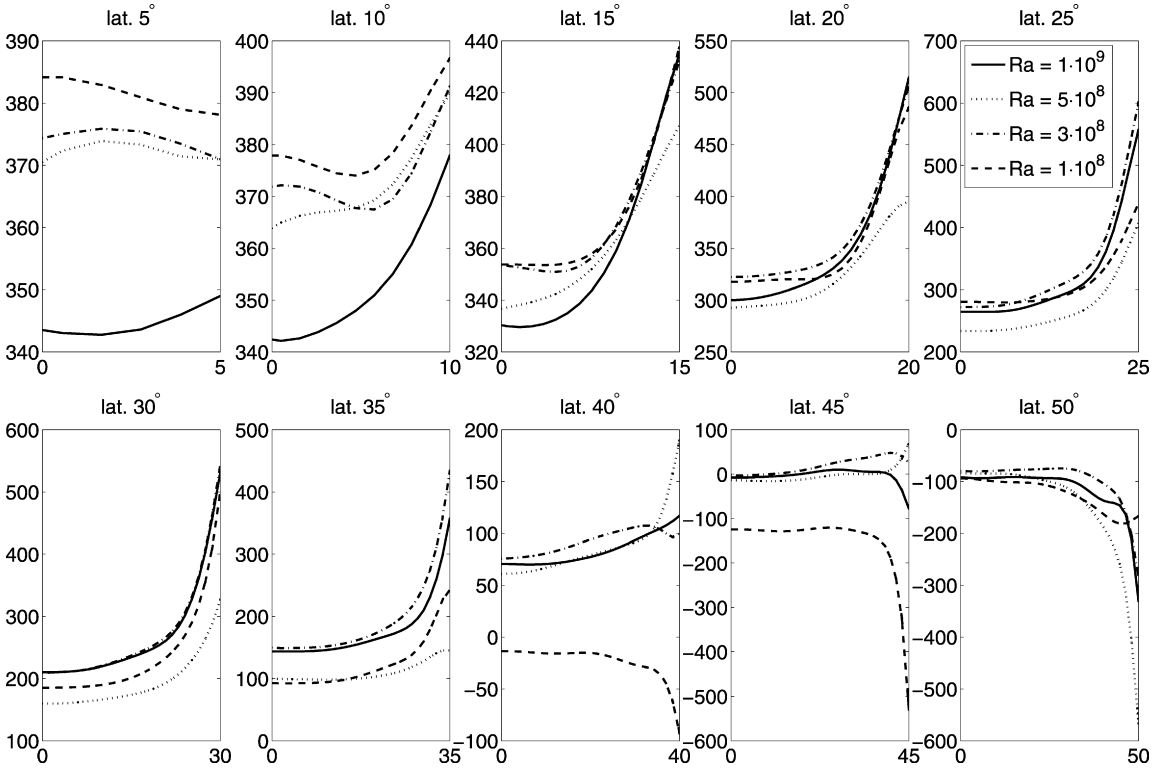

Fig. 20. Zonally averaged zonal velocity ($\mathrm{m\,s^{-1}}$) along slices parallel to the axis of rotation. Each slice goes from the outer surface (denoted by the latitude where the slice intersects the outer surface) to the equatorial plane. Similar velocity profiles are shown for four experiments with different Rayleigh numbers of 1×10^9, 5×10^8, 3×10^8 and 1×10^8; other parameters are set equal in all runs ($Ek = 1.5 \times 10^{-4}$ and $Pr = 10$). The velocity is scaled by Rayleigh number ratio to show the similarity of the profiles, although the magnitudes differ. The velocity values ($\mathrm{m\,s^{-1}}$) on the vertical axis are for the run with $Ra_F = 1 \times 10^9$.

levels where the density change is biggest. Consequently the interior zonal velocities are weaker. We find the vertical structure of the zonal winds a robust result for a range of nondimensional model parameters although the amplitude of the winds does depend on the strength of the forcing. This result is different than previous suggestions, which either assumed a deep source for the jets with strong interior velocities or a shallow driving force and weak interior velocities. Therefore solely due to compressible effects we expect to find vertical shear resulting in weaker interior velocities.

The convective rotating flow organizes in coherent rotating structures parallel to the axis of rotation. For weaker convection (smaller Rayleigh and Prandtl numbers) these columns are more regular (Kaspi, 2008), though we find the general structure of these columns for the more turbulent cases as well (Fig. 14). These convective eddy structures drive eddy angular momentum fluxes across surfaces of constant angular momentum, and therefore transfer angular momentum to the exterior of the planet. Convergence of these eddy angular momentum fluxes drives the equatorial superrotation. Eddy heat fluxes on the other hand are also dominant along the axis of rotation and therefore combine with mean heat fluxes to heat the poles. This meridional heat transport may compensate for the stronger solar heating at the equator, giving an overall appearance of uniform meridional temperature structure. Future such anelastic models which will include also the solar forcing would be able to better address this question, and the formation of multiple zonal jets away from the equator. The upcoming JUNO mission to Jupiter would be able to measure to a certain extent the deep circulation (Hubbard, 1999), providing more information on the deep dynamics. Combining these measurements with gravity moment calculations (Kaspi, 2008) using anelastic general circulation models might provide more information on the deep circulation.

Acknowledgments

This work has been supported by NSF grant AST-0708106, funds from the Woods Hole Oceanographic Institution academic program and the NOAA Climate and Global Change Postdoctoral Fellowship Program administrated by the University Corporation for Atmospheric Research. We are grateful to Jean-Michel Campin for his assistance in building the anelastic model. We thank Alan Plumb, Joe Pedlosky, Richard Lindzen, Sara Seager and Tapio Schneider for their comments and suggestions during the preparation of this work, and two anonymous reviewers for their insightful and constructive comments.

References

Adcroft, A., Campin, J.-M., Heimbach, P., Hill, C., Marshall, J., 2007. MITgcm user's manual (online documentation). http://www.mitgcm.org.

Atkinson, D.H., Pollack, J.B., Seiff, A., 1996. Galileo Doppler measurements of the deep zonal winds at Jupiter. Science 272, 842–843.

Aurnou, J.M., Olson, P.L., 2001. Strong zonal winds from thermal convection in a rotating spherical shell. Geophys. Res. Lett. 28 (13), 2557–2559.

Aurnou, J., Heimpel, M., Wicht, J., 2007. The effects of vigorous mixing in a convective model of zonal flow on the ice giants. Icarus 190, 110–126.

Aurnou, J., Heimpel, M., Allen, L., King, E., Wicht, J., 2008. Convective heat transfer and the pattern of thermal emission on the gas giants. Geophys. J. Int. 173, 793–801.

Batchelor, G.K., 1953. The conditions for dynamical similarity of motions of a frictionless perfect-gas atmosphere. Q. J. R. Meteor. Soc. 79, 224–235.

Busse, F.H., 1970. Thermal instabilities in rapidly rotating systems. J. Fluid Mech. 44, 441–460.

Busse, F.H., 1976. A simple model of convection in the jovian atmosphere. Icarus 29, 255–260.

Campin, J.-M., Adcroft, A., Hill, C., Marshall, J., 2004. Conservation of properties in a free-surface model. Ocean Model. 6 (3–4), 221–244.

Cho, J., Polvani, L.M., 1996. The formation of jets and vortices from freely-evolving shallow water turbulence on the surface of a sphere. Phys. Fluids 8, 1531–1552.

Christensen, U.R., 2002. Zonal flow driven by strongly supercritical convection in rotating spherical shells. J. Fluid Mech. 470, 115–133.

Conrath, B.J., Flasar, F.M., Pirraglia, J.A., Gierasch, P.J., Hunt, G.E., 1981. Thermal structure and dynamics of the jovian atmosphere. II. Visible cloud features. J. Geophys. Res. 86, 8769–8775.
Dowling, T.E., Ingersoll, A.P., 1988. Potential vorticity and layer thickness variations in the flow around Jupiter's great red spot and white oval BC. J. Atmos. Sci. 45 (8), 1380–1396.
Dowling, T.E., Ingersoll, A.P., 1989. Jupiter's great red spot as a shallow water system. J. Atmos. Sci. 46 (21), 3256–3278.
Dowling, T.E., Bradley, M.E., Colón, E., Kramer, J., Lebeau, R.P., Lee, G.C.H., Mattox, T.I., Morales-Juberías, R., Palotai, C.J., Parimi, V.K., Showman, A.P., 2006. The EPIC atmospheric model with an isentropic/terrain-following hybrid vertical coordinate. Icarus 182, 259–273.
Durran, D.R., 1989. Improving the anelastic approximation. J. Atmos. Sci. 46, 1453–1461.
Evonuk, M., 2008. The role of density stratification in generating zonal flow structures in a rotating fluid. Astrophys. J. 673, 1154–1159.
Evonuk, M., Glatzmaier, G.A., 2006. A 2D study of the effects of the size of a solid core on the equatorial flow in giant planets. Icarus 181, 458–464.
Fernando, H.J.S., Chen, R.-R., Boyer, D.L., 1991. Effects of rotation on convective turbulence. J. Fluid Mech. 228, 513–547.
Gierasch, P.J., Magalhaes, J.A., Conrath, B.J., 1986. Zonal mean properties of Jupiter's upper troposphere from Voyager infrared observations. Icarus 67, 456–483.
Guillot, T., 2005. The interiors of giant planets: Models and outstanding questions. Annu. Rev. Earth Planet. Sci. 33, 493–530.
Guillot, T., Morel, P., 1995. CEPAM: A code for modeling the interiors of giant planets. Astron. Astrophys. Suppl. Ser. 109, 109–123.
Guillot, T., Stevenson, D.J., Hubbard, W.B., Saumon, D., 2004. The interior of Jupiter. In: Bagenal, F., Dowling, T.E., McKinnon, W.B. (Eds.), Jupiter. The Planet, Satellites and Magnetosphere. Cambridge University Press, pp. 35–57.
Hanel, R., Conrath, B., Herath, L., Kunde, V., Pirraglia, J., 1981. Albedo, internal heat, and energy balance of Jupiter—Preliminary results of the Voyager infrared investigation. J. Geophys. Res. 86, 8705–8712.
Hanel, R.A., Conrath, B.J., Kunde, V.G., Pearl, J.C., Pirraglia, J.A., 1983. Albedo, internal heat flux, and energy balance of Saturn. Icarus 53, 262–285.
Haynes, P.H., Marks, C.J., McIntyre, M.E., Shepherd, T.G., Shine, K.P., 1991. On the downward control of extratropical diabatic circulations by eddy-induced mean zonal forces. J. Atmos. Sci. 48, 651–679.
Heimpel, M., Aurnou, J., 2007. Turbulent convection in rapidly rotating spherical shells: A model for equatorial and high latitude jets on Jupiter and Saturn. Icarus 187, 540–557.
Heimpel, M., Aurnou, J., Wicht, J., 2005. Simulation of equatorial and high-latitude jets on Jupiter in a deep convection model. Nature 438, 193–196.
Hide, R., 1969. Dynamics of the atmospheres of the major planets with an appendix on the viscous boundary layer at the rigid bounding surface of an electrically-conducting rotating fluid in the presence of a magnetic field. J. Atmos. Sci. 26, 841–853.
Holton, J.R., 1992. An Introduction to Dynamic Meteorology, third ed. Academic Press, San Diego.
Hubbard, W.B., 1984. Planetary Interiors. Van Nostrand Reinhold Co., New York. 343 pp.
Hubbard, W.B., 1999. Gravitational signature of Jupiter's deep zonal flows. Icarus 137, 357–359.
Ingersoll, A.P., 1976. Pioneer 10 and 11 observations and the dynamics of Jupiter's atmosphere. Icarus 29, 245–252.
Ingersoll, A.P., 1990. Atmospheric dynamics of the outer planets. Science 248, 308–315.
Ingersoll, A.P., Pollard, D., 1982. Motion in the interiors and atmospheres of Jupiter and Saturn: Scale analysis, anelastic equations, barotropic stability criterion. Icarus 52, 62–80.
Ingersoll, A.P., Porco, C.C., 1978. Solar heating and internal heat flow on Jupiter. Icarus 35, 27–43.
Ingersoll, A.P., Dowling, T.E., Gierasch, P.J., Orton, G.S., Read, P.L., Sánchez-Lavega, A., Showman, A.P., Simon-Miller, A.A., Vasavada, A.R., 2004. Dynamics of Jupiter's atmosphere. In: Bagenal, F., Dowling, T.E., McKinnon, W.B. (Eds.), Jupiter. The Planet, Satellites and Magnetosphere. Cambridge University Press, pp. 105–128.
Kaspi, Y., 2008. Turbulent convection in rotating anelastic spheres: A model for the circulation on the giant planets. Ph.D. thesis, MIT.
Kaspi, Y., Flierl, G.R., 2007. Formation of jets by baroclinic instability on gas planet atmospheres. J. Atmos. Sci. 64, 3177–3194.
Kippenhahn, R., Weigert, A., 1990. Stellar Structure and Evolution, vol. XVI. Springer-Verlag, Berlin. 468 pp., 192 figs. Also in: Astronomy and Astrophysics Library.
Kirk, R.L., Stevenson, D.J., 1987. Hydromagnetic constraints on deep zonal flow in the giant planets. Astrophys. J. 316, 836–846.
Lian, Y., Showman, A.P., 2008. Deep jets on gas-giant planets. Icarus 194, 597–615.
Lindzen, R.S., 1977. Some Aspects of Convection in Meteorology. Lect. Notes in Phys., vol. 71. Springer-Verlag, Berlin, p. 128.
Liu, J.J., Goldreich, P., Stevenson, D., 2007. Constraints on deep-seated zonal winds inside Jupiter and Saturn. ArXiv e-prints, 711.
Marshall, J., Adcroft, A., Hill, C., Perelman, L., Heisey, C., 1997. Hydrostatic, quasi-hydrostatic and nonhydrostatic ocean modeling. J. Geophys. Res. 102 (C3), 5753–5766.
Ogura, Y., Phillips, N.A., 1962. Scale analysis of deep and shallow convection in the atmosphere. J. Atmos. Sci. 19, 173–179.
Orton, G.S., Fisher, B.M., Baines, K.H., Stewart, S.T., Friedson, A.J., Ortiz, J.L., Marinova, M., Ressler, M., Dayal, A., Hoffmann, W., Hora, J., Hinkley, S., Krishnan, V., Masanovic, M., Tesic, J., Tziolas, A., Parija, K.C., 1998. Characteristics of the Galileo probe entry site from Earth-based remote sensing observations. J. Geophys. Res. 103, 22791–22814.
Pedlosky, J., 1987. Geophysical Fluid Dynamics. Springer, Berlin.
Porco, C.C., West, R.A., McEwen, A., Del Genio, A.D., Ingersoll, A.P., Thomas, P., Squyres, S., Dones, L., Murray, C.D., Johnson, T.V., Burns, J.A., Brahic, A., Neukum, G., Veverka, J., Barbara, J.M., Denk, T., Evans, M., Ferrier, J.J., Geissler, P., Helfenstein, P., Roatsch, T., Throop, H., Tiscareno, M., Vasavada, A.R., 2003. Cassini imaging of Jupiter's atmosphere, satellites and rings. Science 299, 1541–1547.
Porco, C.C., Baker, E., Barbara, J., Beurle, K., Brahic, A., Burns, J.A., Charnoz, S., Cooper, N., Dawson, D.D., Del Genio, A.D., Denk, T., Dones, L., Dyudina, U., Evans, M.W., Giese, B., Grazier, K., Helfenstein, P., Ingersoll, A.P., Jacobson, R.A., Johnson, T.V., McEwen, A., Murray, C.D., Neukum, G., Owen, W.M., Perry, J., Roatsch, T., Spitale, J., Squyres, S., Thomas, P., Tiscareno, M., Turtle, E., Vasavada, A.R., Veverka, J., Wagner, R., West, R., 2005. Cassini imaging science: Initial results on Saturn's atmosphere. Science 307, 1243–1247.
Rhines, P.B., 1975. Waves and turbulence on a beta plane. J. Fluid Mech. 69, 417–443.
Saumon, D., Chabrier, G., van Horn, H.M., 1995. An equation of state for low-mass stars and giant planets. Astrophys. J. 99, 713–741.
Schneider, T., Liu, J.J., 2009. Formation of jets and equatorial superrotation on Jupiter. J. Atmos. Sci. 66, 579–601.
Scott, R.K., Polvani, L.M., 2007. Forced-dissipative shallow-water turbulence on the sphere and the atmospheric circulation of the giant planets. J. Atmos. Sci. 64, 3158–3176.
Scott, R.K., Polvani, L.M., 2008. Equatorial superrotation in shallow atmospheres. Geophys. Rev. Lett. 35, doi:10.1029/2008GL036060. 24202.
Seiff, A., Kirk, D.B., Knight, T.C.D., Young, L.A., Milos, F.S., Venkatapathy, E., Mihalov, J.D., Blanchard, R.C., Young, R.E., Schubert, G., 1997. Thermal structure of Jupiter's upper atmosphere derived from the Galileo probe. Science 276, 102–104.
Showman, A.P., 2007. Numerical simulations of forced shallow-water turbulence: Effects of moist convection on the large-scale circulation of Jupiter and Saturn. J. Atmos. Sci. 64, 3132–3157.
Showman, A.P., Dowling, T.E., 2000. Nonlinear simulations of Jupiter's 5-micron hot spots. Science 289, 1737–1740.
Showman, A.P., Gierasch, P.J., Lian, Y., 2006. Deep zonal winds can result from shallow driving in a giant-planet atmosphere. Icarus 182, 513–526.
Smith, K.S., 2003. A local model for planetary atmospheres forced by small-scale convection. J. Atmos. Sci. 61, 1420–1433.
Sun, Z.-P., Schubert, G., Glatzmaier, G.A., 1993. Banded surface flow maintained by convection in a model of the rapidly rotating giant planets. Science 260, 661–664.
Vasavada, A.R., Showman, A.P., 2005. Jovian atmospheric dynamics: An update after Galileo and Cassini. Rep. Prog. Phys. 68, 1935–1996.
Williams, G.P., 1978. Planetary circulations. 1. Barotropic representation of the jovian and terrestrial turbulence. J. Atmos. Sci. 35, 1399–1426.
Williams, G.P., 1979. Planetary circulations. 2. The jovian quasi-geostrophic regime. J. Atmos. Sci. 36, 932–969.
Yamazaki, Y.H., Skeet, D.R., Read, P.L., 2004. A new general circulation model of Jupiter's atmosphere based on the UKMO unified model: Three-dimensional evolution of isolated vortices and zonal jets in mid-latitudes. Planet. Space Sci. 52, 423–445.
Zhang, K., Schubert, G., 1996. Penetrative convection and zonal flow on Jupiter. Science 273, 941–943.